JGR Solid Earth

RESEARCH ARTICLE
10.1029/2018JB016352

Shear Wave Splitting Discloses Two Episodes of Collision-Related Convergence in Western North America

Lei Wu[1,2,3], **Yu J. Gu**[1], **Yunfeng Chen**[1], **and Huaying Liang**[2]

[1]Department of Physics, University of Alberta, Edmonton, Alberta, Canada, [2]CAS Key Laboratory of Mineralogy and Metallogeny, Guangzhou Institute of Geochemistry, Chinese Academy of Sciences, Guangzhou, China, [3]Earth Dynamics Research Group, The Institute for Geoscience Research, School of Earth and Planetary Sciences, Curtin University, Perth, Western Australia, Australia

Abstract Seismic anisotropy imposes first-order constraints on the strain history of crust and upper mantle rocks. In this study, we analyze the mantle seismic anisotropy of the Western Canada Sedimentary Basin using a new shear wave spitting data set consisting of 1,333 teleseismic arrivals from 82 seismic stations. The resulting 332 high-quality measurements yield a regional mean apparent splitting time (i.e., the magnitude of anisotropy) of 1.1 ± 0.3 s and an average fast orientation (i.e., the direction of anisotropy) of 54.6° ± 17.2°, which favor a two-layer anisotropic model based on the 90° back azimuthal periodicity in both parameters. The northeast trending fast orientations dominate the lower layer at lithospheric depths and are approximately parallel to the present-day absolute plate motions (APMs; i.e., <35°) due to the active asthenospheric flow. On the other hand, deviations from the APMs along the Canadian Rocky Mountain foothills could reflect disrupted mantle flow surrounding a southwestward migrating cratonic lithosphere. Also revealed are two elongated upper-layer anisotropic anomalies in the lithosphere that are spatially correlated with Moho depths. Their characteristics suggest frozen-in anisotropy imprinted along two convergent boundaries: (1) the Paleoproterozoic Snowbird Tectonic Zone that separates northeast (north) from northwest (south) fast directions and (2) the foothills of the Rocky Mountains that exhibit northeast trending orientations consistent with those of the APMs, maximum crustal stress, and electromagnetic anisotropy. Compressions associated with the Cordilleran orogenesis could be responsible for the spatial changes in the shear wave anisotropy from the foothills to the cratonic interior.

Key Points:
- New shear wave splitting results disclose layered anisotropy beneath the western Laurentia
- Differential splitting times from two-layer anisotropic modeling are correlated with Moho depths, suggesting crustal impact on the shear wave splitting observations across Alberta
- The upper-layer fossil anisotropic fabrics reveal two collision-related convergent events that formed the western North America

Supporting Information:
- Supporting Information S1

Correspondence to:
L. Wu,
lei.wu@curtin.edu.au;
lei.wu@ualberta.ca

Citation:
Wu, L., Gu, Y. J., Chen, Y., & Liang, H. (2019). Shear wave splitting discloses two episodes of collision-related convergence in western North America. *Journal of Geophysical Research: Solid Earth*, *124*. https://doi.org/10.1029/2018JB016352

Received 13 JUL 2018
Accepted 15 FEB 2019
Accepted article online 21 FEB 2019

1. Introduction

1.1. Geological Overview of the Alberta Basin

The Alberta Basin, the largest deposition center in the Western Canada Sedimentary Basin (WCSB), is a relatively thin, northeastward trending wedge of supracrustal rocks tapering on, or juxtaposed with, Precambrian crystalline rocks (Bally et al., 1966; Beaumont, 1981; Mossop & Shetsen, 1994; Price, 1981). The basin is geologically bounded to the east by the 2.0- to 1.8-Ga Trans-Hudson Orogen (THO), a Paleoproterozoic orogenic belt that extends from the northern United States to eastern Canada (Corrigan et al., 2009; Darbyshire et al., 2017; Hoffman, 1988; Zhao et al., 2002). Directly west of this basin is the Canadian Rockies, a portion of the North American Cordillera that was initiated by extensional tectonics in the earliest Cambrian period followed by convergent tectonics and subsequent Mesozoic and Cenozoic collisional events (Coney et al., 1980; Johnston, 2008; Liu et al., 2010; Monger & Price, 2002). The basement of the Alberta Basin was initially assembled during the Paleoproterozoic tectonic amalgamation of western Laurentia (Hoffman, 1988; Ross, 2002; Ross et al., 1991) and subsided through later-stage interactions between the North American craton and the Cordilleran orogen during the Mesozoic times (e.g., Late Jurassic and Late Cretaceous; DeCelles, 2004; Johnston, 2008; Monger & Price, 2002).

The basement framework in Alberta largely consists of Archean cratons (i.e., Rae, Hearne, and Medicine Hat Block [MHB]) and Paleoproterozoic terranes (i.e., Buffalo Head Terrane, Chinchaga, Wabamum, and Lacombe terranes), magmatic arcs (i.e., Rimbey and Ksituan terranes), and orogens (i.e., Taltson orogen and THO) (Figure 1a; e.g., Hoffman, 1988; Ross, 2002; Ross et al., 1991). The Rae and Hearne provinces are separated by the Snowbird Tectonic Zone (STZ), an ~2,800-km geological structure that extends from the foothills of the Canadian Cordillera through the exposed Canadian Shield to Hudson Bay (Berman et al., 2007; Hoffman, 1988; Ross, 2002). The STZ likely represents a ca. 1.9-Ga suture (Berman et al.,

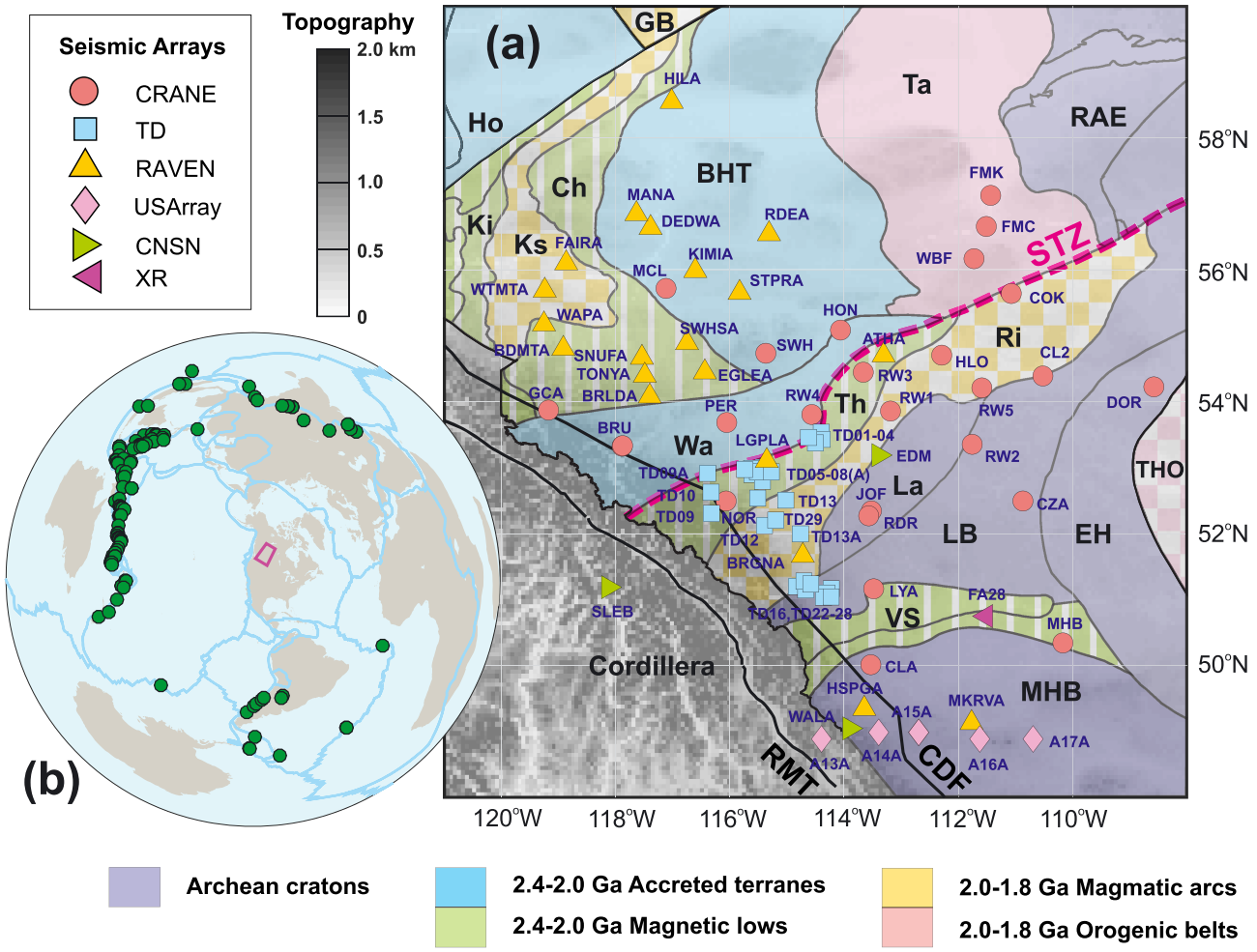

Figure 1. (a) Simplified geologic map showing the seismic stations network. The topography is from the global relief model ETOPO1 (Amante & Eakins, 2009). The colored shadings delineate three major western Laurentia Archean continental fragments (i.e., Rae, Hearne, and the Medicine Hat Block from north to south), which are separated by two main discontinuities: the Snowbird Tectonic Zone (pink dashed line) in the north and the Vulcan structure in the south. The gray contours denote the component tectonic units of the three continental fragments. Abbreviations and acronyms: BHT = Buffalo Head Terrane; CDF = Cordilleran Deformation Front; Ch = Chinchaga; EH = Eyehill High; GB = Great Bear; Ho = Hottah; Ki = Kiskatinaw; Ks = Ksituan; La = Lacombe; LB = Loverna Block; MHB = Medicine Hat Block; Ri = Rimbey; RMT = Rocky Mountains trench; STZ = Snowbird Tectonic Zone; Ta = Taltson; Th = Thorsby; THO = Trans-Hudson Orogen; Wa = Wabamun; VS = Vulcan structure. (b) Azimuthal equidistance map showing the distribution of earthquake events (green dots) in this study. The map is rotated such that all land masses are shown. The light blue lines indicate the present-day plate boundaries (Bird, 2003). The purple polygon denotes our studied area in (a).

2007; Gu et al., 2018; Hoffman, 1988), though alternative origins such as a ca. 2.6-Ga intracontinental shear zone (Hanmer et al., 1995) or a ca. 2.55-Ga incipient rift (Flowers et al., 2006) remain debated. The Wabamun domain northwest of the STZ collided with the Hearne province after the closing of a remnant oceanic basin represented by the Thorsby magnetic low (Ross et al., 2000; Figure 1a). The Rimbey terrane, a juxtaposed aeromagnetic high, may have formed as a magmatic belt during the southeastward subduction beneath Hearne (Chen et al., 2017; Eaton & Cassidy, 1996; Gu et al., 2018; Ross et al., 1991, 2000). Coeval with the consumption of the Thorsby basin, the westward underthrusting of the THO caused lithosphere-scale compressional deformation in the Hearne lithosphere (Ross et al., 2000). In southern Alberta, the Loverna Block in the Hearne province might have amalgamated with the Archean MHB along the Vulcan structure during the Proterozoic era (Eaton et al., 1999; Gu et al., 2018; Ross et al., 1991) or possibly in the Archean (Clowes et al., 2002; Gorman et al., 2002). As a critical suture zone in this regional collisonal framework, the Vulcan structure bears distinctive signatures highlighted by anomalous potential field (Ross, 2002), north dipping mantle seismic reflections (Clowes et al., 2002;

Gorman et al., 2002), and abrupt changes in both seismic velocity (Chen et al., 2017) and electric resistivity (Nieuwenhuis et al., 2014) at lithospheric depths.

1.2. Previous Geophysical Studies and Seismic Anisotropy

Over the past few decades, the Alberta Basin has been one of the most intensively studied regions thanks to oil and gas exploration, Lithoprobe active-source experiments (e.g., Clowes et al., 2002; Cook, 1995; Eaton et al., 2000; Gorman et al., 2002; Hope et al., 1999; Ross et al., 2000), and, more recently, broadband seismic surveys (Bao & Eaton, 2015; Chen et al., 2015; Dalton et al., 2011; Gu et al., 2011, 2015, 2018). These studies offer compelling evidence for intricate domains below the sedimentary basin, which largely support an earlier-proposed regional Proterozoic tectonic framework (e.g., Pilkington et al., 2000; Ross et al., 1991; Villeneuve et al., 1993) and a Cenozoic sharp structural gradient from the stable continental cratons east of the Alberta Basin to the Canadian Cordillera (e.g., Chen et al., 2017, 2018; Nettles & Dziewoński, 2008; van der Lee & Frederiksen, 2005). Recent seismological evidence further suggests that much of the past and ongoing deformation has been engraved onto the underlying lithosphere and upper mantle, contributing to mantle fabrics that are largely parallel to the present-day absolute plate motion (APM) directions based on surface wave tomography (e.g., Bao et al., 2016; Gung et al., 2003; Marone & Romanowicz, 2007; Yuan & Romanowicz, 2010) and shear wave splitting observations (e.g., Bastow et al., 2011; Courtier et al., 2010; Currie et al., 2004; Gu et al., 2011; Liu et al., 2014; Shragge et al., 2002).

Based on the crustal-scale imbrication with opposing dips along the STZ and the THO, Ross et al. (2000) propose that western Laurentia was assembled as the result of the Paleoproterozoic tectonic entrapment of the Hearne craton by the Wabamun domain (NW) and the THO (SE). Recent work suggests that this prolonged convergence could have existed across the collisional system comprising Hearne, MHB, and Wyoming (hereafter the HMW tectonic system; Gu et al., 2018), considering (1) the similar ages (i.e., 1.85–1.70 Ga) of the basement domains (Ross et al., 1991), (2) the ca. 1.87-Ga subduction-related gneiss and the 1.77 Ga granulite facies metamorphism along the Great Falls Tectonic Zone that welded the MHB and the Wyoming craton (e.g., Mueller et al., 2002; Sims et al., 2005), and (3) the thickened crust and increased Vp/Vs ratios near the boundaries of the three component domains. Both tectonic models predict northwesterly lithospheric fabrics across central eastern Alberta that formed during the Paleoproterozoic assembly of western Laurentia.

These northeast trending fabrics at both crustal and upper mantle levels have been documented by recent geophysical surveys across the Alberta Basin. Specifically, shear wave splitting studies have shown the overall northeast trending seismic anisotropy in western North America in possible connection with the present-day APM of North America; the lateral deviations from the northeasterly orientation are related to the Paleoproterozoic convergence associated with the amalgamation of western Laurentia (Courtier et al., 2010; Currie et al., 2004; Gu et al., 2011; Liu et al., 2014; Shragge et al., 2002). This is further confirmed by surface wave tomographic results that reveal northwest trending fabrics at 150- to 200-km depths, possibly preserved from the assembly of western Laurentia (Bao et al., 2016; Yuan & Romanowicz, 2010). At the crustal level, strain fabrics from the anisotropy of magnetic susceptibility (Turner & Gough, 1983), borehole breakouts (e.g., Bell & Bachu, 2003; Reiter et al., 2014), and earthquakes' focal mechanisms (e.g., Wang et al., 2017) suggest similar northeast directed maximum crustal stress orientations, which are approximately perpendicular to the fold-and-thrust belt of the Rocky Mountains. The origin of the crustal anisotropy has been linked to topographic loading, variations in the lithospheric thickness and density, and basal tractions associated with mantle flow (e.g., Flesch et al., 2007). Also revealed is northeast directed midcrustal electrical anisotropy, which may have originated from episodes of domain accretion and the postcollisional shortening along the northwest (e.g., Boerner et al., 2000; Nieuwenhuis et al., 2014).

1.3. Motivation of this Study

Data undersampling of the Alberta Basin has posed a major challenge to validating the regional lithosphere deformation history, which has likely involved substantial thermal and tectonic overprinting of various tectonic domains since their initial assembly during the Paleoproterozoic era (Aulbach et al., 2004; Chen et al., 2015; Hoffman, 1988; Mahan & Williams, 2005; Ross et al., 1991; Ross & Eaton, 2002). Based on the similar basement rock ages (i.e., 1.85–1.70 Ga; e.g., Clowes et al., 2002; Mueller et al., 2002; Mueller & Frost, 2006; Ross et al., 1993; Villeneuve et al., 1993) and the common crustal characteristics (i.e., depressed Moho and

high *Vp*/*Vs* ratios), Gu et al. (2018) proposed that convergent tectonics dominated across the HMW tectonic system, where a similar lithospheric strain imprints were predicted. However, due to insufficient surface geological exposure and seismic data coverage, there are many questions surrounding the nature and crustal/mantle expressions of major geological structures in the WCSB. For example, observational support for the impact of the Paleoproterozoic "tectonic vise" and dual subduction (Clowes et al., 2002; Ross et al., 2000) has been elusive along the STZ. A related but unresolved issue is the origin of the similarly oriented surface plate velocities (e.g., Gripp & Gordon, 2002; Kreemer et al., 2014), stress field (e.g., Heidbach et al., 2016; Reiter et al., 2014; Wang et al., 2017), midcrustal electrical anisotropy (e.g., Boerner et al., 2000; Nieuwenhuis et al., 2014), and seismic anisotropy in the lithosphere and upper mantle (e.g., Courtier et al., 2010; Gu et al., 2011; Shragge et al., 2002). While plate boundary forces and body forces associated with the surface motion of the North American plate likely play a key role in the mantle dynamics (e.g., Bell & Bachu, 2003; Bell & Gough, 1979; Courtier et al., 2010; Currie et al., 2004; Gu et al., 2011; Reiter et al., 2014; Shragge et al., 2002), the origin of the northeast oriented directions within the crust and mantle remains enigmatic for the WCSB region.

The main objective of this study is to examine the seismic anisotropy through the observations and modeling of shear wave spitting, which is a physical phenomenon in which a polarized shear wave splits into a fast and a slow shear waves by an anisotropic medium, similar to the optical birefringence of minerals under polarized light (Bowman & Ando, 1987; Silver & Chan, 1991). The associated splitting parameters consist of a delay time between the fast and slow polarizations and a fast orientation (azimuth), which are sensitive functions of the strength and orientation of receiver-side anisotropy assuming that silicate perovskite maintains an isotropic texture during deformation and recrystallization in the lower mantle (e.g., Anderson, 2007; Long & Silver, 2009). Shear wave splitting provides a unique tool for probing the relationship between deformation and anisotropy (e.g., Crampin et al., 1984; Long & Becker, 2010; Savage, 1999; Silver, 1996). It is frequently assumed that the anisotropy of most parts of the mantle is dominated by lattice-preferred orientation (e.g., Crampin et al., 1984; McKenzie, 1979), that is, a preferred distribution of individually anisotropic mineral grains that are (re)aligned by historical and present-day mantle circulation (Fouch & Rondenay, 2006; Savage, 1999; Silver, 1996). Other sources of anisotropy include the alignment of isotropic elastic materials including crustal melt pockets and cracks (Crampin & Chastin, 2003; Long & Becker, 2010), quartz layers in shear zones (e.g., Ward et al., 2012), and strain associated with fracture propagation (e.g., Leary et al., 1987) and/or linearized seismic anomalies (e.g., Cimini & De Gori, 2001; Ökeler et al., 2009). Compared with oceanic anisotropy that is dominated by asthenospheric flow (e.g., Becker et al., 2003; Conrad et al., 2007), subcontinental anisotropy is often a superposition of fossil (or frozen) anisotropy in the lithosphere and contemporary flow-related anisotropy in the asthenosphere (e.g., Bastow et al., 2011; Bokelmann & Silver, 2002; Darbyshire et al., 2013; Gao & Liu, 2009; Liddell et al., 2017; Park & Levin, 2002; Reed et al., 2017).

In this study, we analyze a broadband seismic data set consisting of 1,333 shear wave phases from six regional networks, which is the largest of this region to date. Since early 2006, the regional seismic station coverage in Alberta has improved substantially through the establishment of the Canadian Rockies and Alberta Network (hereafter CRANE), the first semiuniform broadband seismic array in Alberta and parts of Saskatchewan, Canada (Gu et al., 2011). Continuous seismic signals from this array have laid the groundwork for a number of recent findings pertaining to regional seismicity and crust/mantle structures (e.g., Bao et al., 2016; Chen et al., 2015, 2018; Gu et al., 2018), some of which are considered in this analysis for the assessment of past and ongoing lithosphere deformation processes beneath the Alberta Basin.

2. Data and Methods

2.1. Data and Splitting Measurements

This study utilizes 120 earthquake recordings from six regional networks, including the CRANE, TransAlta Dam Monitoring Network (hereafter TD), Regional Alberta Observatory for Earthquake Studies Network (hereafter RAVEN), USArray Transportable Array, the Canadian National Seismic Network (CNSN), and the Florida to Edmonton Seismic Experiment (hereafter XR) array (Figure 1). Specifically, we analyzed data from 27 CRANE stations, 27 TD stations, 20 RAVEN stations, 3 CNSN permanent stations (EDM, SLEB, and WALA), and nearby temporary deployments from the USArray (five stations) and XR networks (one station;

see Figure 1). The 82 combined stations provide a semiuniform coverage in central and southern Alberta (Figure 1a; see Table S2 for the list of stations and events). Most of these stations (have) operated continuously for at least 2 years, recording an average of 16 large earthquakes with the moment magnitude Mw ≥6.25 for a detailed examination of shear wave splitting (Figure 1b). The CRANE stations have been active since 2006; the TD and RAVEN stations began deployment in 2013; the CNSN stations were established in 1993; and the USArray and XR stations operated in 2007–2009 and 2001–2002, respectively. The reader is referred to Table S1 and Figure S1 for detailed information about the seismic networks and the associated instrument responses of representative stations. Depending on station operation periods, our analyzed earthquakes are restricted to those within an Mw range of 6.25–8.00 and an epicenter range of 90–130°. The event catalog contains no major temporal gaps: Most years it features multiple satisfactory earthquakes (>3), except for 2002–2006 during which only a single event was retained per year. For the final measurements we incorporated 1,333 shear wave core phases consisting of SKS, pSKS, sSKS, SKKS, and SKiKS arrivals.

In this analysis, each measurement was made using the Silver and Chan (1991) method (hereafter the SC method). After the removal of instrument response along with constant and linear trends, we band-pass-filtered the three-component time series in the north-east-vertical (hereafter N-E-Z) coordinate system with corner frequencies of 0.02 and 0.2 Hz. We selected this frequency range empirically to ensure robust SKS/SKKS arrivals (see also section 2.2). The resulting seismograms were then rotated to the ray-coordinate-based L-Q-T system, where the positive longitudinal component L points along the ray path toward the station, the positive Q component points toward the earthquake, and the transverse component T is 90° counterclockwise away from the positive Q component (Wüstefeld et al., 2008). The subsequent step involved the search for the optimal splitting parameters and associated errors from the time domain covariance matrix of the horizontal particle motion. Optimal splitting parameters obtained from this method either (1) maximize the largest eigenvalue of the covariance matrix for the corrected fast and slow seismograms or (2) minimize the energy on the corrected transverse component if the initial polarization direction is known (for core phases such as the SKS and SKKS arrivals, the initial polarization direction should follow their back azimuths). Hereafter, we refer to the two methods as the eigenvalue and minimum energy approaches, respectively. For quality control and null detection on each measurement, we also carried out the splitting analysis using the rotation correlation method (Bowman & Ando, 1987; hereafter the RC method). This alternative single-record method searches for the optimal splitting parameters that maximize the cross-correlation coefficient (i.e., similarity) between two corrected seismogram components (i.e., Q and T components). Both the preprocessing and splitting measurements were performed using the freeware SplitLab (Wüstefeld et al., 2008). Figure 2 illustrates representative splitting measurements and their diagnostic plots for determining the optimal pair of fast orientation and delay time at the 95% confidence level from the input seismograms in the N-E-Z coordinate system.

It is worth noting that a null measurement results if (1) there is a lack of horizontal anisotropy or (2) if the fast axis is parallel to or normal to the back azimuth, where minimal energy is expected on the uncorrected transverse component and the horizontal particle motion is initially (quasi-)linearized (e.g., Long & Silver, 2009). The issue with the latter scenario is the 90° ambiguity in the fast axis estimate. To address the issue, we compute the fast orientation difference $|\Delta\phi| = |\phi_{SC} - \phi_{RC}|$) and the split time ratio ($\rho = \frac{\delta t_{RC}}{\delta t_{SC}}$; Wüstefeld & Bokelmann, 2007) based on the pair of splitting parameters from the RC and SC methods to provide a quantitative approach for splitting/null distinction and quality assessment for each measurement.

To ensure the quality and robustness of the results, we only accept measurements with the signal-to-noise ratio (SNR) greater than 5 and error bounds less than 35° at the 95% confidence level. In this study we adopt the Wüstefeld and Bokelmann (2007) approach to detect null measurements and to perform quality control. Specifically, we consider a measurement to be a null direction if $32° < |\Delta\phi| < 58°$ and $\rho < 0.3$; we deem a measurement robust if the angular difference$|\Delta\phi| < 22.5°$ and the split time ratio $\rho > 0.7$ (Wüstefeld & Bokelmann, 2007). Results acquired using either of the two SC approaches (minimum energy or eigenvalue, whichever yields less error) are retained, and the remaining measurements (that failed to meet all of the aforementioned criteria) are rejected.

To verify the stability of the measurements and the robustness of the data, we select 15 stations that recorded clear SKS phases for an event in East Caroline Islands, Micronesia, at a depth of 13 km (2014.215.00.17.03,

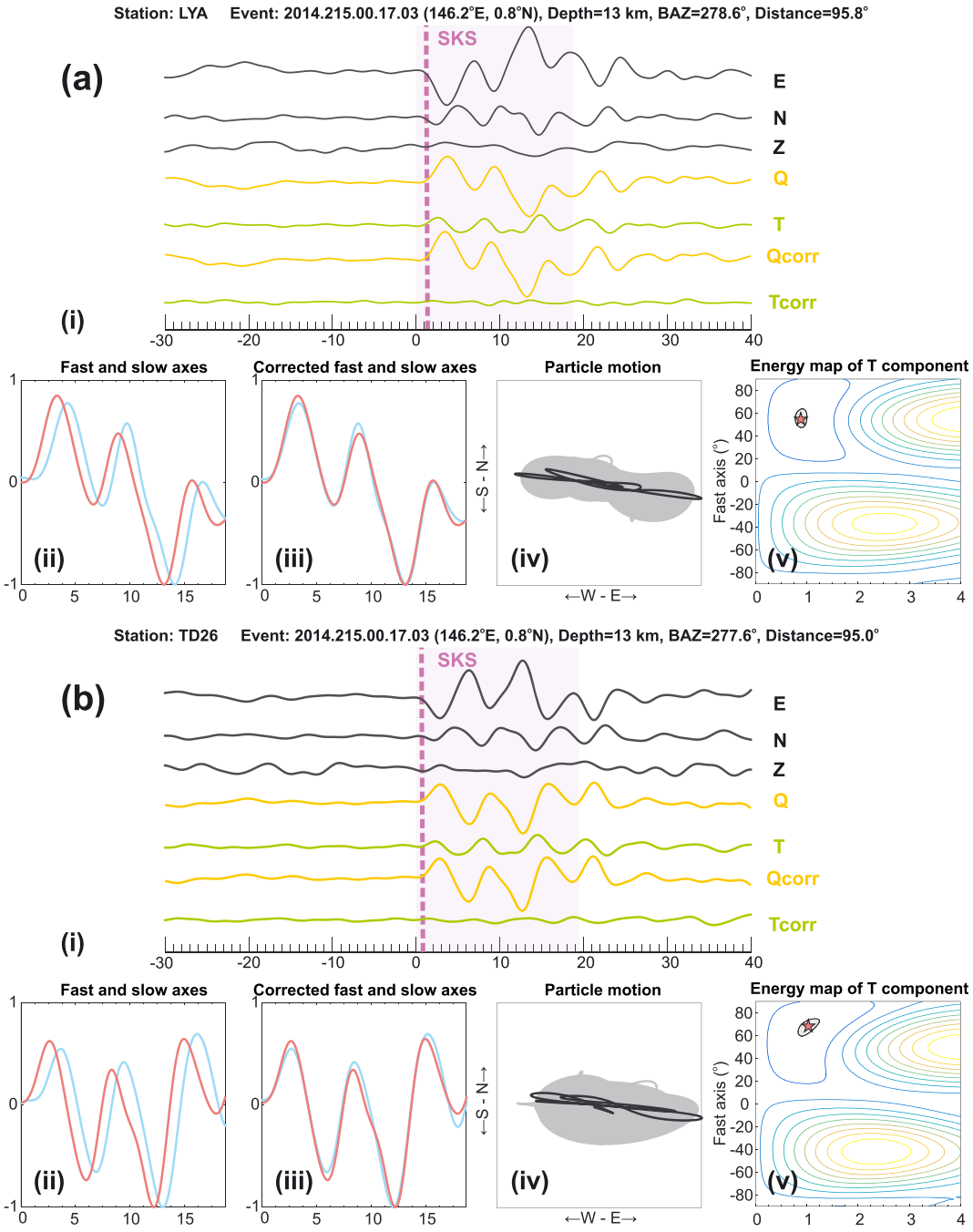

Figure 2. Representative splitting measurements. (i) Original seismogram components in the N-E-Z coordinate system (black lines). Also shown are Q and T seismograms (colored lines) that are both before and after correcting the waveform and split time differences between fast and slow polarizations. (ii and iii) Fast (red) and slow (blue) waveforms before and after correcting the time delay. (iv) Horizontal particle motions with (black line) and without (gray line) correcting for the split parameters. (v) Contour map of the energy of the corrected transverse component where the optimal splitting parameters associated with the minimum energy and the 95% confidence interval are indicated by the pink star and gray shading, respectively.

146.2°E, 0.8°N; Figure 3). These original seismograms were first filtered with corner frequencies of 0.02 and 0.2 Hz and then rotated into the L-Q-T coordinate system (Figure 3). The resulting radial (Q) and transverse (T) components were aligned on the predicted SKS arrival times according to the iasp91 Earth model (Kennett & Engdahl, 1991). Clear and coherent SKS waveforms are clearly identified from the two components, especially from the T component seismogram (Figure 3), indicating that the variable SKS phases are

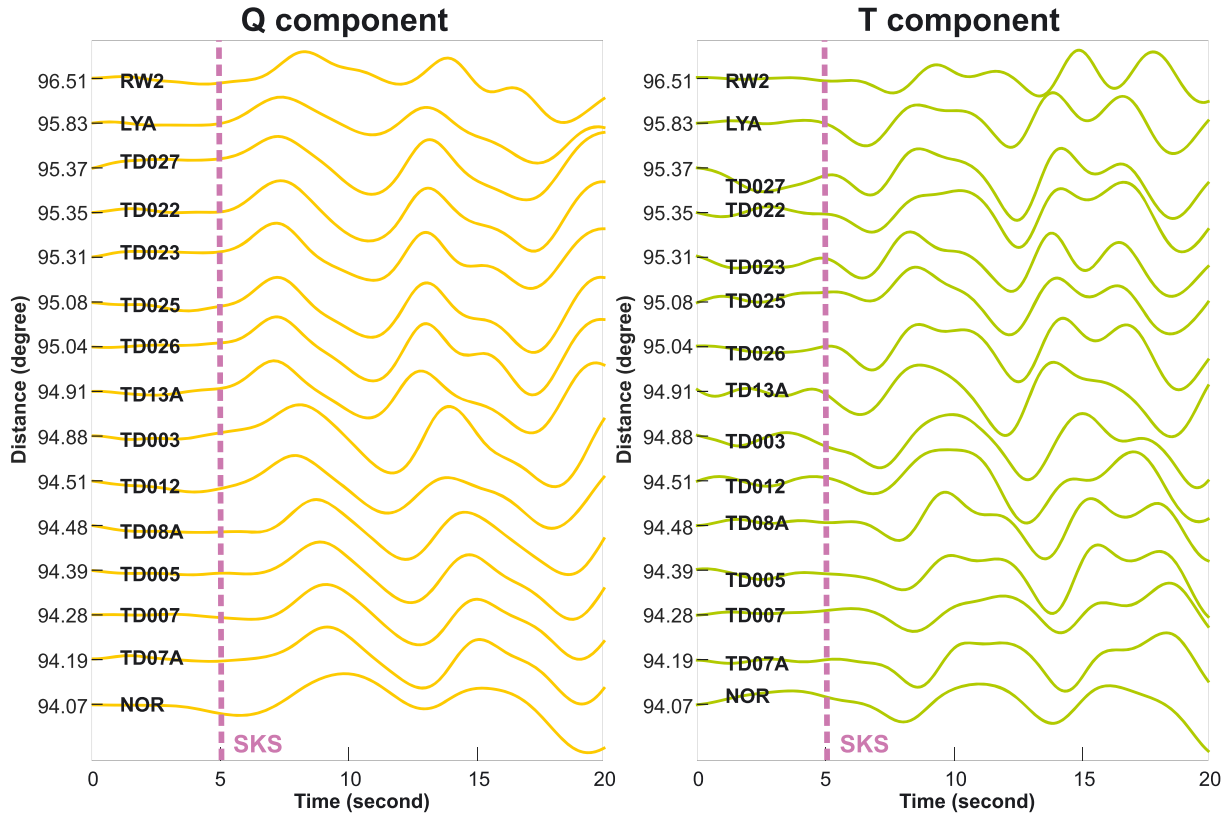

Figure 3. Seismogram components (left) Q and (right) T for event East Caroline Islands in Micronesia (2014.215.00.17.03, 146.2°E, 0.8°N) at a depth of 13 km. Seismograms are arranged by epicentral distance and aligned on SKS phases whose expected arrival times according to the iasp91 Earth model (Kennett & Engdahl, 1991) are marked by the purple dashed line.

associated with anisotropy rather than background noises or null measurements. In the latter scenario, the initial amplitude of the T component is close to 0. It is also worth noting that some SKS waveforms are complicated by the trailing pSKS phase and/or sSKS phase. In such cases we adjusted the analysis window length to 20 s to ensure that complete, peak-to-peak SKS phases were included for the final measurements. The reader is referred to Figure 2 for the representative splitting measurements where the energy on the T seismograms is minimized.

2.2. Modeling of Layered Anisotropy

Shear wave splitting provides a powerful tool for investigating the receiver-side anisotropy but has poor depth resolution due to the integrated effect of anisotropy along the ray path (Marone & Romanowicz, 2007). To obtain more depth control, we applied a grid search method to model the apparent variations in splitting parameters as a function of back azimuth (Silver & Savage, 1994). The modeling recovered the anisotropic fabrics in the presence of two or multiple anisotropic layers. The step sizes of the grid search were 1.0° for ϕ and 0.1 s for δt. The best fit multilayer models were found by minimizing the misfit function χ^2 (Gao & Liu, 2009).

$$\chi^2 = \frac{1}{N}\sum\left[w_1\times\left(\frac{\phi_i^{\mathrm{a}}-\phi_i^{\mathrm{m}}}{\Delta\phi_i^{\mathrm{a}}}\right)^2 + w_2\times\left(\frac{\delta t_i^{\mathrm{a}}-\delta t_i^{\mathrm{m}}}{\Delta\delta t_i^{\mathrm{a}}}\right)^2\right]$$

where $\Delta\phi_i^{\mathrm{a}}$ and $\Delta\delta t_i^{\mathrm{a}}$ represent errors in the ith pair of apparent splitting parameters ϕ_i^{a} and δt_i^{a} from a given station, whose weighting factors are assigned as $w_1 = 0.8$ and $w_2 = 0.2$ (Reed et al., 2017), respectively. Depending on wave types (i.e., longitudinal or transverse) and propagation paths, our analyzed core phases pSKS, SKiKS, SKKS, SKS, and sSKS exhibited typical periods of 7, 8, 5, 7, and 7 s, respectively. We therefore adopted a dominant frequency of 0.15 Hz (Silver & Savage, 1994), which is the average of the analyzed shear

wave phases. Following Gao and Liu (2009), we rescaled the resulting misfits by their minimum values using $\frac{\chi^2-\chi^2_{min}}{\chi^2_{min}}$ and then calculated the "mean" optimal two-layer fits along with their standard deviations from models with rescaled misfits no larger than 1.0.

We performed a grid search for two-layer anisotropic models on stations with at least six reliable nonnull measurements. Given the linear strain fabrics at both crustal and upper mantle levels (see section 1.2 for the summary of regional geological, geophysical, and seismic anisotropy observations), we assumed that the apparent splitting resulted from a combination of lithospheric fossil anisotropy and viscous shear in the underlying asthenosphere due to the present-day motion of the North American plate (Fouch & Rondenay, 2006; Liu et al., 2014; Marone & Romanowicz, 2007; Savage, 1999; Silver, 1996).

The splitting modeling was carried out using the function "MS_effective_medium" from freeware MSAT (Walker & Wookey, 2012). This choice was motivated partially by the simplicity of the method and partially by recent reports of a two-layer lithosphere overlying the asthenosphere beneath the WCSB containing (1) a top layer comprising chemically distinct and depleted Archean cores (i.e., Rae, Hearne, and the MHB) as well as the surrounding Paleoproterozoic orogenic belts (Bao et al., 2016; Currie et al., 2004; Gu et al., 2011; Yuan & Romanowicz, 2010) and (2) a lower thermally conductive layer that possibly formed after the amalgamation of western Laurentia (Gung et al., 2003; Yuan & Romanowicz, 2010). However, we do not consider such complexity here because the depths of anisotropy are poorly constrained by shear wave splitting measurements and the associated modeling efforts.

3. Shear Wave Splitting Results

A total of 1,333 core transiting teleseismic shear wave phases were investigated for the splitting analysis, yielding 332 measurements with satisfactory SNRs (> 5; see Table S2) that included 259 SKS, 20 pSKS, 10 sSKS, 41 SKKS, and 2 SKiKS arrivals based on the iasp91 Earth model (Kennett & Engdahl, 1991). During the data selection, 239 reliable splits and 10 null splits (hereafter nulls) were detected based on their associated angular difference $|\Delta\phi|$ and splitting time ratio $\frac{\delta t_{RC}}{\delta t_{SC}}$ (see section 2.1), and 83 measurements were rejected either because their error bounds were larger than 35° or because they represented neither reliable splits nor nulls. The high-quality splits from the aforementioned phases yielded statistically indistinguishable fast polarization directions and splitting times, demonstrating the self-consistency of our splitting measurements from different core-transiting phases (Figure S2).

Figure 4a shows the fast orientations from 63 (out of 83) high-quality stations employed in this study (Table 1). The majority of these measurements are directed toward the northeast, which is comparable with the present-day plate motion directions in Alberta (~49–55°) with respect to both the no-net-rotation (NNR) reference frame (Kreemer et al., 2014) and the hotspot frame HS3-NUVEL1A (Gripp & Gordon, 2002). The NNR frame defines a space where the velocities of the lithospheric plates are relative to the Earth's deep interior (a.k.a. the mesosphere, which is the presumed strong deep mantle beneath the weak asthenosphere; Harper, 1986) and appears to predict comparable motions of North America from HS3-NUVEL1A (Gripp & Gordon, 2002). The robustness of our measurements is further corroborated by the comparable splitting results from a few USArray stations deployed near the southern portion of the Canadian Rocky Mountain foothills that also exhibit the APM-dominated fast orientations (Liu et al., 2014; Figure 4a). In addition, the maximum shear strain in the upper mantle inferred from the apparent fast polarizations appears to be oriented along the maximum compressive crustal stress directions. Figure 4b illustrates a compilation of focal mechanisms of six local earthquakes with Richter magnitude ~4 (Wang et al., 2017), 153 records from the recent Canadian stress database (Reiter et al., 2014) and 79 records from the World Stress Map Database Release 2016 (https://www.world-stress-map.org/) (Heidbach et al., 2016). The maximum horizontal compressive stress orientations from the stress database and the moment tensors yield medians of 47.0° and 48.0° relative to geographic north, respectively, with approximately 90.0° directional complexity adjacent to the Cordilleran Deformation Front bounded between the Cordilleran foreland fold-and-thrust belt and the Alberta Basin (Figure 4b). It has been suggested that the consistently northeast trending stress orientations result from both surface topography and deeper effects such as mantle flow and variations in lithospheric thickness (Reiter et al., 2014, and references therein).

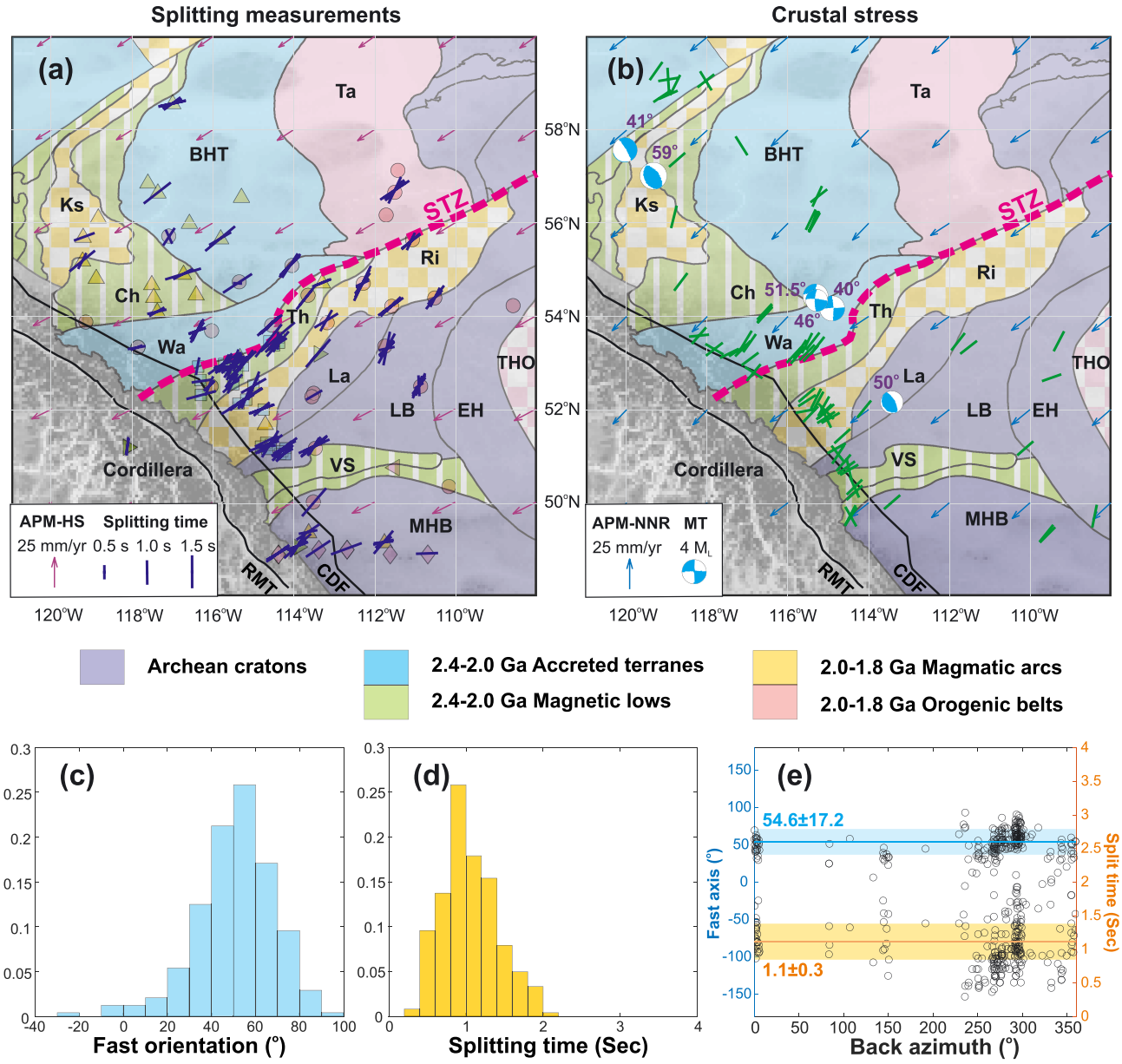

Figure 4. (a) The splitting measurements after selection, where bars are oriented with the fast polarization and are scaled with the time delay. Also shown is the present-day velocity field with respect to the hotspot (HS) reference frame (Gripp & Gordon, 2002; purple arrows). Abbreviations, acronyms, and conventions as in Figure 1. (b) Maximum crustal compressive stress directions according to focal mechanisms (beach balls) for six local earthquakes (Wang et al., 2017) and a combination of 153 records (pink bars) from the recent update of the Canadian stress database (Reiter et al., 2014) and 79 entries (green bars) from the World Stress Map Database Release 2016 (https://www.world-stress-map.org/; Heidbach et al., 2016). Blue arrows represent the present-day absolute plate motion (APM) directions based on the no-net-rotation (NNR) reference frame (Kreemer et al., 2014). Distribution of (c) fast orientations and (d) split times from robust measurements after the data selection. (e) Variations in the fast orientation (blue dots) and split time (orange dots) with back azimuth, where error bounds of these splitting parameters are not shown for clarity. The blue (orange) line and shading denote the regional average fast orientation (split time) and associated standard deviation.

Figures 4c and 4d show histograms of fast orientation and delay time for the selected splitting measurements after rejecting low-quality and null measurements. Both fast polarizations and delay times exhibit the Gaussian distribution with mean values of 54.6° ± 17.2° and 1.1 ± 0.3 s (Figure 4e), respectively. There seem to be multiple anisotropic layers beneath Alberta, as seen in the periodic variations in fast polarizations and time delays as a function of back azimuth (Figure 5). Previous studies have demonstrated that a 180° back azimuthal periodicity is diagnostic of a dipping anisotropic layer (Chevrot, 2000) and that a 90° back

Table 1
Statistics of Robust Splitting Measurements (Table S2) at the Station Level

Station	Slong (°E)	Slat (°N)	ϕ_m (°)	δt_m (s)	*n/N*	Station	Slong (°E)	Slat (°N)	ϕ_m (°)	δt_m (s)	*n/N*
A13A	−114.4	48.9	60.4 ± 3.3	1.2 ± 0.1	4/4	RW2	−111.7	53.3	44.0 ± 15.3	0.9 ± 0.3	13/18
A14A	−113.4	49.0	60.1 ± 0.0	1.4 ± 0.0	1/2	RW3	−113.7	54.4	42.7 ± 0.9	1.2 ± 0.3	2/2
A15A	−112.7	49.0	72.3 ± 0.0	1.6 ± 0.0	1/3	RW4	−114.6	53.8	49.3 ± 5.3	1.0 ± 0.4	8/13
A16A	−112.7	49.0	—	—	0/0	RW5	−111.6	54.2	55.2 ± 4.5	1.0 ± 0.3	8/10
A17A	−110.7	48.9	88.3 ± 0.0	1.1 ± 0.0	1/1	SLEB	−118.1	51.2	9.1 ± 4.8	0.8 ± 0.1	2/3
ATHA	−113.3	54.7	70.3 ± 0.9	0.9 ± 0.1	2/2	SNUFA	−117.5	54.7	—	—	0/0
BDMTA	−118.9	54.8	—	—	0/1	STPRA	−115.8	55.7	58.8 ± 6.2	1.5 ± 0.4	2/2
BR2	−117.9	53.3	—	—	0/0	SWH	−115.4	54.7	76.5 ± 22.6	1.1 ± 0.8	2/3
BRGNA	−114.7	51.7	—	—	0/0	SWHSA	−116.8	54.9	70.3 ± 6.9	1.5 ± 0.5	2/2
BRLDA	−117.4	54.1	71.3 ± 10.4	0.9 ± 0.1	2/3	TD01	−114.4	53.6	28.2 ± 35.7	1.3 ± 1.2	2/2
BRU	−117.9	53.3	76.4 ± 7.3	0.8 ± 0.2	2/2	TD02	−114.4	53.4	32.9 ± 22.3	0.7 ± 0.4	9/9
CL2	−110.5	54.4	44.3 ± 11.5	1.0 ± 0.3	4/5	TD03	−114.5	53.4	43.0 ± 8.2	0.7 ± 0.3	3/9
CLA	−113.5	50.0	44.8 ± 0.0	1.7 ± 0.0	1/1	TD04	−114.6	53.5	42.9 ± 0.0	1.9 ± 0.0	1/4
COK	−111.1	55.6	45.0 ± 12.7	0.8 ± 0.3	6/7	TD05	−115.4	53.0	50.0 ± 17.9	0.8 ± 0.1	4/8
CZA	−110.9	52.5	27.9 ± 18.5	0.8 ± 0.3	9/16	TD06	−115.6	53.0	71.2 ± 0.0	1.6 ± 0.0	1/1
DEDWA	−117.4	56.6	56.0 ± 0.0	1.6 ± 0.0	1/1	TD06A	−115.5	53.0	46.7 ± 15.7	1.2 ± 0.3	5/6
DOR	−108.6	54.2	—	—	0/0	TD07	−115.6	52.9	79.5 ± 14.8	1.3 ± 0.1	2/4
EDM	−113.4	53.2	45.6 ± 0.6	1.4 ± 0.5	2/2	TD07A	−115.7	53.0	48.2 ± 10.9	1.1 ± 0.4	5/5
EGLEA	−116.4	54.5	—	—	0/0	TD08	−115.4	52.8	37.9 ± 1.2	1.5 ± 0.4	2/3
FA28	−111.5	50.8	—	—	0/0	TD08A	−115.3	53.0	42.7 ± 6.5	1.2 ± 0.5	6/6
FAIRA	−118.9	56.1	—	—	0/1	TD09	−116.3	52.3	76.7 ± 0.0	1.5 ± 0.0	1/1
FMC	−111.5	56.7	48.1 ± 8.2	1.1 ± 0.3	12/19	TD09A	−116.4	52.9	12.2±0.0	0.8 ± 0.0	1/2
FMK	−111.4	57.1	—	—	0/1	TD10	−116.3	52.6	83.1 ± 0.0	1.0 ± 0.0	1/1
GCA	−119.2	53.9	—	—	0/0	TD11	−115.5	52.6	52.5 ± 16.0	0.9 ± 0.3	4/5
HILA	−117.0	58.6	72.7 ± 9.8	1.2 ± 0.2	5/5	TD12	−115.4	52.1	59.7 ± 4.0	1.2 ± 0.5	3/3
HLO	−112.3	54.7	45.0 ± 13.3	0.9 ± 0.4	8/9	TD13	−115.0	52.5	39.2 ± 21.3	1.3 ± 0.2	3/5
HON	−114.1	55.1	45.6 ± 6.1	1.2 ± 0.3	4/7	TD13A	−114.8	52.0	67.6 ± 9.2	1.1 ± 0.3	4/4
HSPGA	−113.7	49.4	69.9 ± 14.5	1.1 ± 0.3	2/2	TD16	−114.8	51.2	72.0 ± 0.0	1.3 ± 0.0	1/2
JOF	−113.5	52.3	63.2 ± 0.0	0.9 ± 0.0	1/1	TD22	−114.2	51.2	58.9 ± 4.4	1.2 ± 0.3	3/4
KIMIA	−116.6	56.0	—	—	0/0	TD23	−114.3	51.1	60.6 ± 10.1	0.9 ± 0.3	4/4
LGPLA	−115.4	53.1	—	—	0/1	TD24	−114.4	51.0	—	—	0/0
LYA	−113.5	51.2	56.3 ± 10.3	1.1 ± 0.3	15/19	TD25	−114.7	51.2	71.9 ± 19.5	1.1 ± 0.1	2/3
MANA	−117.6	56.9	—	—	0/0	TD26	−114.7	51.3	67.6 ± 0.0	1.0 ± 0.0	1/1
MCL	−117.1	55.7	4.8 ± 46.3	0.8 ± 0.2	2/4	TD27	−114.2	51.1	55.3 ± 7.6	0.9 ± 0.2	3/3
MHB	−110.2	50.3	—	—	0/0	TD28	−114.6	51.3	54.0 ± 11.8	1.1 ± 0.2	7/7
MKRVA	−111.8	49.1	66.6 ± 18.6	1.1 ± 0.2	4/4	TD29	−115.2	52.2	49.0 ± 16.0	1.3 ± 0.5	6/6
NOR	−116.1	52.5	42.9 ± 15.6	0.7 ± 0.2	3/10	TONYA	−117.5	54.4	—	—	0/1
PER	−116.4	53.7	50.4 ± 16.3	0.8 ± 0.3	10/19	WALA	−113.9	49.1	57.6 ± 13.8	1.0 ± 0.3	9/10
RDEA	−115.3	56.6	—	—	0/0	WAPA	−119.3	55.2	42.8 ± 17.0	1.2 ± 0.5	2/2
RDR	−113.6	52.3	—	—	0/0	WBF	−111.7	56.2	—	—	0/0
RW1	−113.2	53.9	47.6 ± 21.2	1.2 ± 0.2	2/4	WTMTA	−119.2	55.7	72.2 ± 0.0	1.1 ± 0.0	1/2

Note. *N* and *n* denote the numbers of splitting measurements before and after rejecting low quality and/or null measurements, respectively.

azimuthal periodic variation in the apparent splitting parameters suggests multiple anisotropic layers (Silver & Savage, 1994). In other words, a monotonous distribution of splitting parameters is expected if the adopted shear wave phases result from a single layer of anisotropy beneath a given receiver with a horizontal axis of symmetry (Silver & Savage, 1994). To unveil the nature of the observed periodicity, we calculate the station averages and standard deviations from individual measurements (Tables 1 and S2), which are not stacked using procedures that implicitly assume a single horizontal anisotropic layer beneath receivers (Wolfe & Silver, 1998). Given that a similar earthquakes distribution is used at each station (Figures 4e and 5), back azimuthal variations in apparent splitting across the recording arrays, which are confirmed by stations with at least six independent measurements (Figure 5), reflect seismic anisotropy at lithosphere depths rather than the outcomes of a common lower mantle anomaly (Long & Silver, 2009). To derive geologically sensible two-layer scenarios from the apparent splitting results, we assume a larger time delay associated with the lower anisotropic layer (i.e., a dominating contribution from asthenospheric shear strain to the apparent splitting), primarily because high-quality fast polarizations across most of

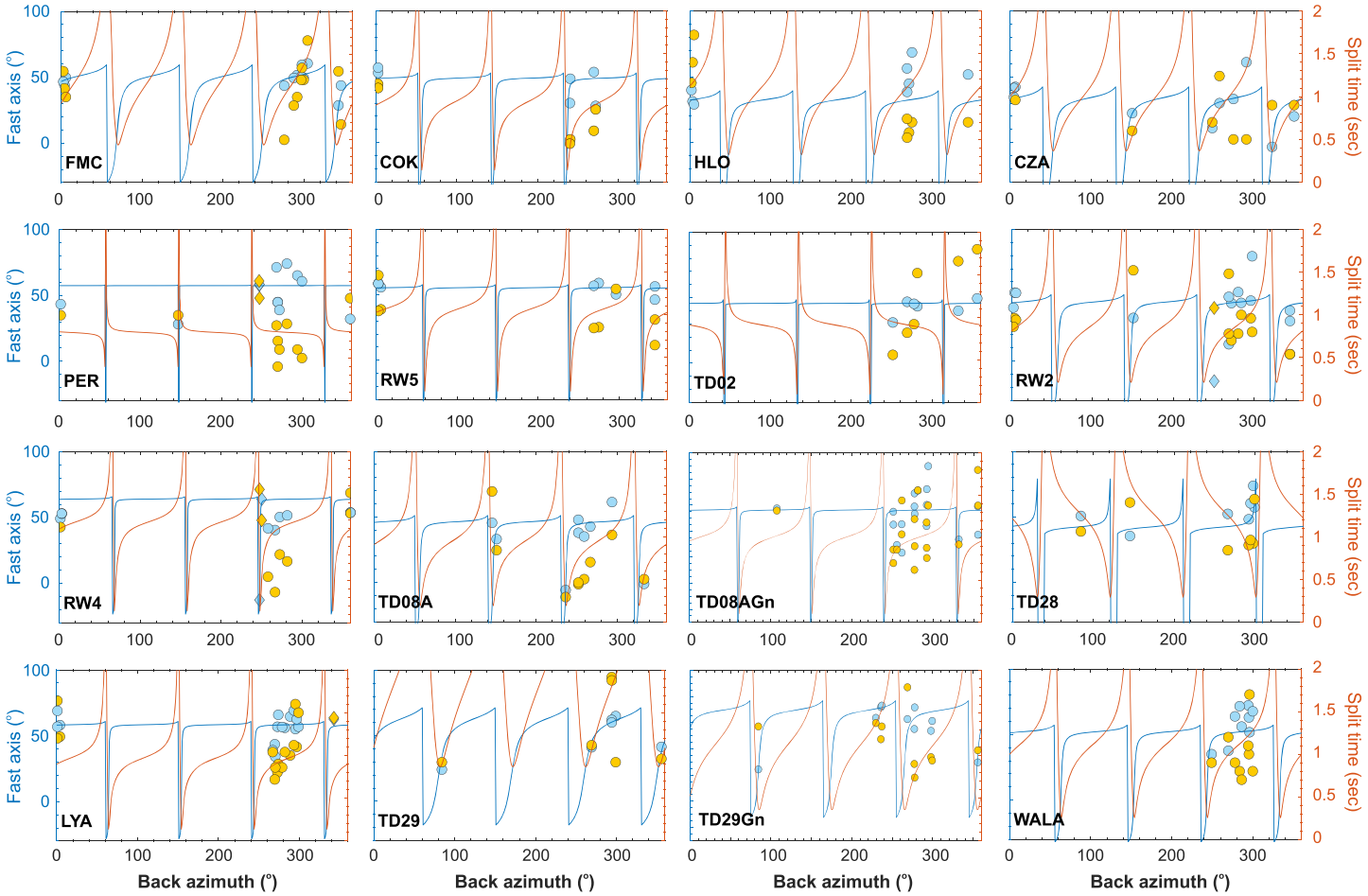

Figure 5. Variations in apparent fast orientations (ϕ) and split times (δt) as a function of back azimuth for stations with at least six splitting measurements. Circles and diamonds denote splitting and null measurements, respectively, whose error bounds are not shown for clarity. The blue and orange curves indicate best fit two-layer anisotropy models for fast orientations and split times, respectively. Modeled splitting parameters (ϕ, δt) along with associated misfits (χ^2) for both upper (U) and lower (L) layers are indicated above each plot.

Alberta (except its southern portion covered by the USArray stations) are overall comparable with regional plate motion directions (Figures 4a and 4e). Unfortunately, our adopted multilayer approach based on ray path integration provides no depth constraints on modeled anisotropic layers (Silver & Savage, 1994).

4. Discussion

4.1. Layered Anisotropic Fabrics Beneath Alberta

Figure 5 shows the best fit two-layer anisotropy model with minimum misfits χ^2 derived from the back azimuthal variations in apparent splitting parameters. The quality of two-layer modeling hinges on the sufficiency of back azimuth coverage of input splitting measurements. Consequently, we exclude from further analysis the two-layer result from station WALA that is derived from splitting data concentrated in only one quadrant (~240–300°) of the splitting-back azimuthal variability diagram (Figure 5). Apparent splitting measurements from stations FMC, COK, CZA, LYA, RW5, TD02, TD08A, TD28, and TD29 are distributed in at least two quadrants and can therefore be reasonably well explained by two-layer anisotropy models, evidenced by their small misfits ($\chi^2 \leq 1.0$; Figure 5). These stations are distributed across a large area in Alberta extending from the southern Taltson magmatic zone through the STZ to the southern Canadian Rockies (Figure 6a), providing first-order constraints on the geometry and strength of anisotropy. On the other hand, two-layer anisotropic results for stations HLO, PER, RW2, and RW4 yield misfits larger than 1.0. This

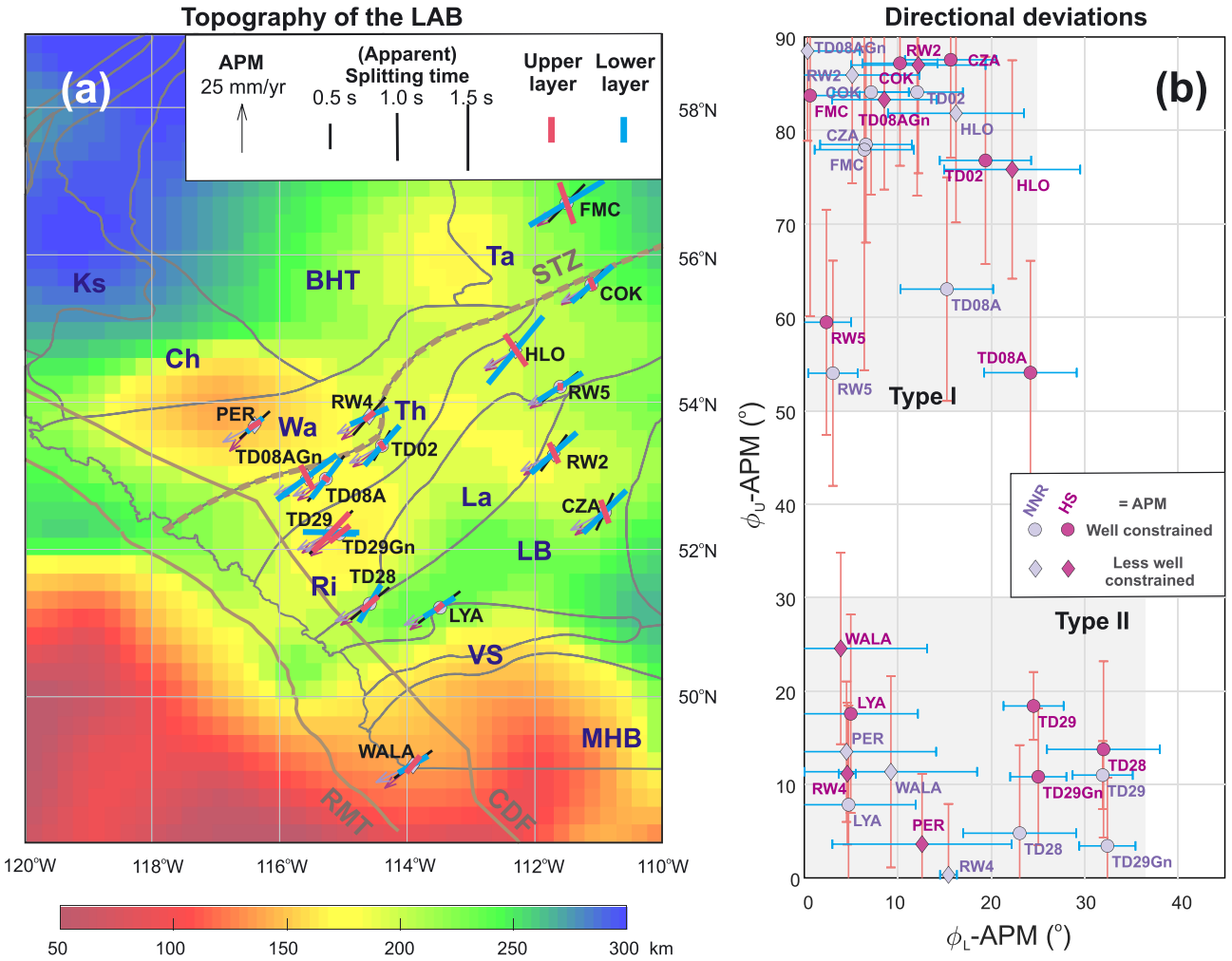

Figure 6. (a) Layered fast polarizations and absolute plate motion (APM) directions superimposed on the topography of the lithosphere-asthenosphere boundary (LAB; Pasyanos et al., 2014). The black bars indicate station averages in this study, and the red/blue bars denote splitting parameters for upper/lower layers in two-layered anisotropy scenarios. The light and dark purple arrows show the present-day APM directions in the no-net-rotation (NNR; Kreemer et al., 2014) and hotspot (HS; Gripp & Gordon, 2002) frames, respectively. Abbreviations, acronyms, and conventions as in Figure 1. (b) Discrepancies between APM directions and fast polarizations in the upper/lower layers at stations with at least six splitting measurements. The light and dark purple markers denote discrepancies in the NNR and HS frames, respectively. Vertical and horizontal error bars denote standard deviations associated with upper-layer and lower-layer fast orientations, respectively. Two-layer results with $\chi^2_{min} \leq 1.0$ and with $\chi^2_{min} > 1.0$ are indicated by circles and diamonds, respectively.

indicates that their errors associated with the modeling are larger than those from individual splitting measurements (Table S2). For instance, the large misfit $\chi^2 = 2.1$ associated with the two-layer result of station HLO is mainly caused by the relatively large variations among the apparent fast orientations within small ranges of back azimuth (see Figure 5). These splits represent robust measurements with careful visual quality inspection and satisfactory SNR values (≥5). However, future studies will need more high-quality splitting measurements from HLO and adjacent areas to verify whether the observed splitting variations with back azimuths are caused by more complex anisotropic structures. For the current study we excluded all two-layer splitting results with misfits greater than 1.0.

It is worth noting that consistency between adjacent stations is an important criterion to evaluate the reliability and stability of the two-layer modeling results. To this end, we grouped adjacent stations with a total of ≥6 measurements and calculated their best fit models (Figure 5). Only stations located in the same tectonic blocks were combined such that the back azimuthal variability of splitting parameters can be related to the underlying layered anisotropic fabrics. Following this procedure, we combined stations adjacent to TD08A (i.e., TD05, TD06, TD06A, TD07, and TD07A) to form a single gather (hereafter

TD08AGn); a similar summary station TD29Gn was formed using nearby stations TD12, TD13, and TD13A (Figure 5). The resulting best-fit two-layer splitting parameters for TD08AGn and TD29Gn are self-consistent with individual station results from TD08A and TD29, respectively. The average discrepancies in fast polarizations and in time delays are merely 4.3° and 0.4 s (Figure 5), respectively, suggesting stable and robust two-layer anisotropy modeling results. Due to insufficient data, station TD25 in the vicinity of TD28 was not analyzed. Measurements from stations TD22– TD27 were not included in the two-layer anisotropy modeling analysis due to the lack of azimuthal variability (their back azimuths were concentrated on ~300°E ± 10°E).

It has long been suggested that shear wave splitting is a result of fossil anisotropy in the upper mantle preserving historical deformation in the lithosphere and active flow in the asthenosphere induced by present-day plate motions (Bokelmann & Silver, 2002; Fouch & Rondenay, 2006; Long & Becker, 2010; Long & Silver, 2009; Marone & Romanowicz, 2007; Savage, 1999; Silver, 1996). To help investigate deformation origins for the anisotropic fabrics beneath the WCSB (Figure 6a), we plotted the differential directions between mean fast polarizations of modeled upper/lower anisotropic layers beneath the selected stations and their surface plate motion directions from both the NNR reference frame (Kreemer et al., 2014) and the hotspot frame HS3-NUVEL1A (Gripp & Gordon, 2002; Figure 6b). These mean-optimal two-layer results with the associated uncertainties were derived from all possible two-layer fits with rescaled misfits $\frac{\chi^2-\chi^2_{\min}}{\chi^2_{\min}} \leq 1.0$ (see section 2.2). Mean-optimal lower-layer fast polarization orientations consistently showed an overall agreement with (i.e., angle differences <35°) the present-day APM directions in both NNR and hotspots reference frames (Gripp & Gordon, 2002; Kreemer et al., 2014) (Figures 6a and 6b), indicative of the entrained fast axes of individual olivine crystals (i.e., lattice-preferred orientation) due to active asthenospheric shear strain associated with the surface plate motion (Long & Becker, 2010; Long & Silver, 2009). It is worth noting that the mean-optimal lower-layer anisotropic results are better constrained than their upper-layer counterparts in the two-layer modeling, as seen from their smaller standard deviations (Figure 6b). The better constrained lower-layer parameters reflect the source of anisotropy predominantly in the asthenosphere, whereas the less well constrained upper-layer parameters are likely indicative of anisotropy associated with multiple sources at various depths (e.g., crustal and upper mantle anisotropy).

Larger variations in the upper-layer anisotropic directions reveal two types of strain fabrics with distinct deformation origins beneath Alberta. The first type of upper-layer anisotropic fabrics is revealed underneath stations COK, CZA, FMC, HLO, RW2, RW5, TD02, TD08A, and TD08AGn and features mostly northwesterly fast polarizations at high angles to the present-day plate motion directions (i.e., ~50.0–90.0°; Figure 6b). The associated anisotropic layer appears to dominate in the blocks/terranes adjacent to the STZ, extending from the Taltson magmatic arc, through the Thorsby magnetic lows and the eastern Rimbey magmatic arc, to the Loverna Block in the Hearne province (Figure 6a). This anisotropy could represent fossil strain fabrics either inherited from the formation of those lithospheric domains or reworked by the compressional forces during the Paleoproterozoic suturing and orogenesis (Ross, 2002; Ross et al., 2000). This northwest trending pattern is consistent with the azimuthal anisotropy constrained by surface wave tomography at crustal and upper lithospheric depths (i.e., periods of 25–70 s; Bao et al., 2016). However, our two-layer results do not support the north directed azimuthal anisotropy at greater depths (i.e., the 70- to 150-s periods) from Bao et al. (2016); in fact, their results significantly deviate from the APM-induced active shear in the asthenosphere (Figure 6a).

The second type of upper-layer anisotropic fabrics is characterized by the fast polarization orientations that are at low angles to both the lower-layer fast orientations and the APM directions (<35°; Figure 6b). This end-member of anisotropic fabrics appears in stations PER, RW4, TD28, TD29, TD29Gn, LYA, and WALA and seems to dominate in the Wabamun terrane northwest of the STZ and adjacent to the southern Canadian Rocky Mountain foothills south of Thorsby. Except for a less well constrained station PER, upper-layer anisotropic fabrics from the remaining stations featured consistently smaller discrepancies away from APM directions in the NNR frame (Figure 6b). This NNR frame is based on geodetic measurements and accounts for intraplate deformation (Kreemer et al., 2014). In comparison, hotspot frame HS3-NUVEL1A is relatively simplified in that it assumes rigid plate motions (Gripp & Gordon, 2002) and could potentially be biased by contemporary hotspot motions as well. We therefore give more credence to APM predictions in the NNR frame for stations that are adjacent to the fold-and-thrust belt in the Canadian Rockies, where

contemporary intercontinental deformation has been well documented by geodetic and geological observations (e.g., Monger & Price, 2002).

It is worth noting that the lower-layer fast orientations beneath three well-constrained stations TD28, TD29, and TD29Gn east of the Cordilleran Deformation Front deviate from the surface APM directions by ~20–35° (Figures 6a and 6b). In comparison, the upper-layer anisotropic fabrics beneath these stations are approximately parallel to the contemporary northeast trending compressional strain in the crust that is derived from recent regional stress databases (Heidbach et al., 2016; Reiter et al., 2014) and focal mechanisms (Wang et al., 2017). Given the topographic complexity of the lithosphere-asthenosphere boundary (LAB) at the western edge of Rimbey and Loverna along the Rocky Mountains foothills (Figures 6a and S3), the variability of lower-layer fast orientations suggests that hot asthenospheric material could be locally trapped where the mantle flow is disrupted by the undulating LAB. In other words, the complex lower-layer anisotropy along the foothills results from the active shear due to both the present-day plate motions and disrupted flow at LAB depths. This is supported by the geodynamic modeling showing that the mantle flow can be significantly flexed around the edge of a continental keel—a seismically fast structure that extends to depths of >250 km beneath a stable craton (Fouch et al., 2000; Gu et al., 2011).

4.2. Crustal Impact on the Shear Wave Splitting Across Alberta

By combining previously published results with our station averages (Courtier et al., 2010; Currie et al., 2004; Shragge et al., 2002), we computed apparent station mean splitting time perturbations, a measure of the anisotropic magnitude, by subtracting the regional mean splitting time of 1.1 ± 0.3 s from each of station averages. The perturbations were interpolated on a 0.25° × 0.25° grid using the spline method and then masked such that only interpolated values from grid cells within a radius of 0.5° of the nearest stations are shown (Figure 7). The resulting splitting time perturbations reveals highly variable strain distribution from the southern Canadian Cordillera to the cratonic fragments in western Laurentia (see Figure 7).

Strong apparent anisotropy is revealed in the regions of convergence including the Mesozoic Cordilleran foothills and the southerly concave segment of the Paleoproterozoic STZ, while a smaller apparent strain magnitude is observed in the interior of Hearne and Wabamun (Figure 7). Given that lower-layer anisotropic fabrics are mostly dominated by asthenospheric flow due to APM that shows negligible variations across western Laurentia (section 4.1), these larger apparent splitting times likely originate from fossil strain in the overlying lithosphere due to historical tectonic events (e.g., Bao et al., 2016; Bao & Eaton, 2015; Chen et al., 2015, 2017; Dalton & Gaherty, 2013; DeCelles, 2004; Gu et al., 2018; Hoffman, 1988; Ross et al., 2000; Schulte-Pelkum et al., 2017). In contrast, the origin depths of the upper-layer strain remain enigmatic, because upper-layer splitting times exhibit no correlation with the LAB (correlation coefficients are −0.01 and −0.26 before and after excluding less reliable two-layer results; Figure S4a) but a weak correlation with Moho depths (correlation coefficients are 0.38 and 0.54 before and after excluding less well constrained two-layer results; Figure S4b). Based on regional thermal models and kimberlite xenolith data, Currie et al. (2004) suspect that the upper anisotropy layer beneath WALA could reach depths of 110 to 140 km. Noticeably, apparent station average splitting time perturbations show no preferential variations with the spatial configurations of anisotropic fabrics in the upper and lower layers (Figures 6, 7a, and 7b), which agree with the earlier conjecture that the splitting observations are a function of the number of anisotropic layers in combination with their thicknesses, the alignment fraction of the olivine a-axis, and the layers' geometry such as dip angles (e.g., Silver & Savage, 1994; Walker & Wookey, 2012). Therefore, the small apparent splitting times across central eastern Alberta do not necessarily indicate weak lithospheric deformation in the upper layer (Figure 7a).

Intriguingly, the differential splitting times ($\delta t_L - \delta t_U$) of the upper and lower layers are anticorrelated with the Moho depths from CRUST1.0 (Laske et al., 2013) with the associated correlation coefficient of −0.61, which increased to −0.82 when stations with less well constrained two-layer anisotropic results were excluded (Figure 7c). We also observe (1) a positive correlation between the upper-layer split times (δt_U) and the $\frac{\delta t_U}{\delta t_L}$ ratios (correlation coefficients are 0.70 and 0.86 before and after excluding less reliable two-layer results; Figure S4c) and (2) a positive correlation between the Moho depths and the $\frac{\delta t_U}{\delta t_L}$ ratios (correlation coefficients are 0.65 and 0.76 before and after excluding poorer two-layer results; Figure S4d). We interpret this statistically significant correlation between the relative magnitude of the upper-layer strain (i.e.,

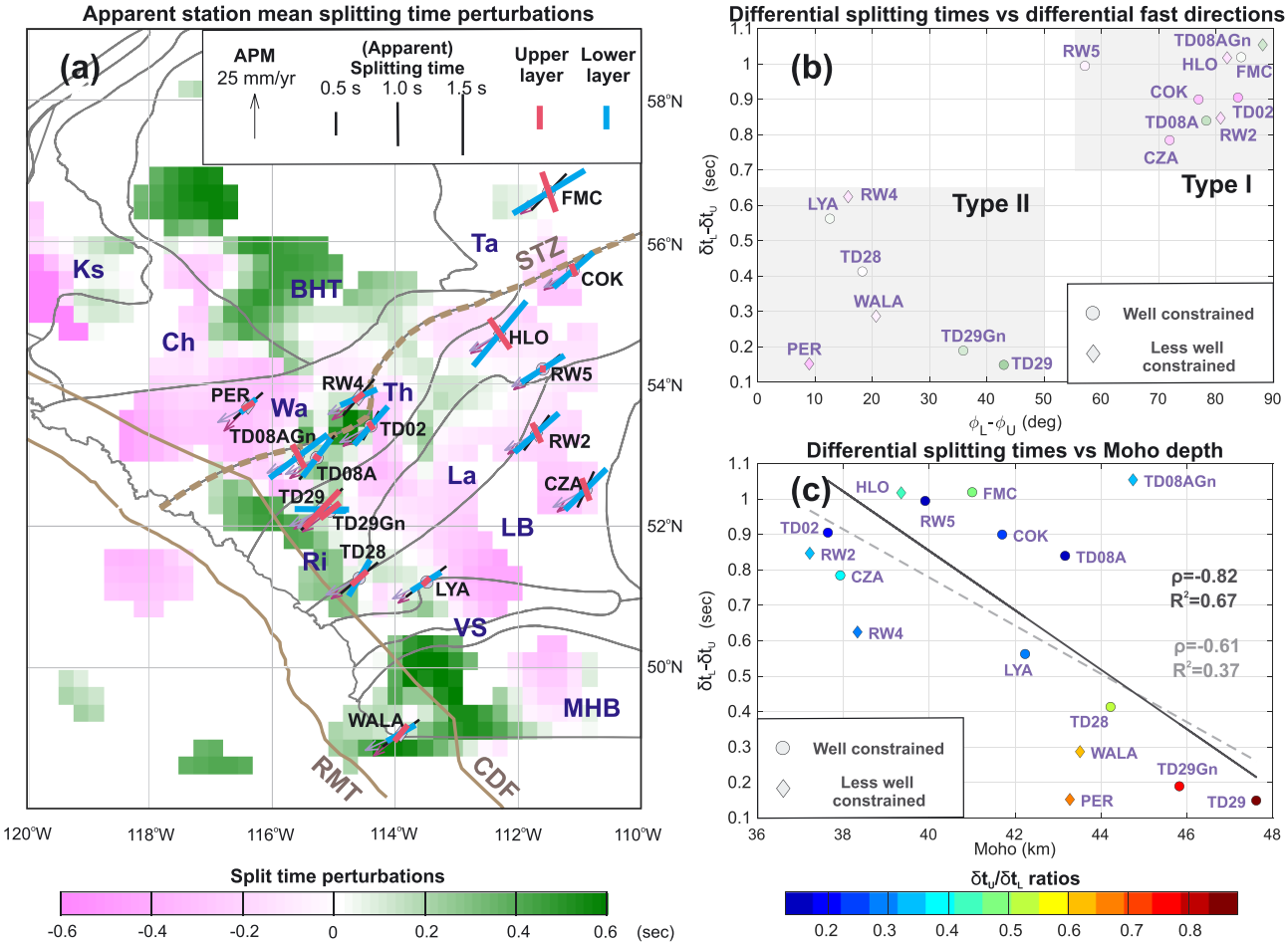

Figure 7. (a) Apparent mean split time perturbations at the station level relative to the regional mean of 1.1 ± 0.3 s as indicated in Figure 4c. Only shown are interpolated values from grid cells within a radius of 0.5° of the nearest stations. Red and blue bars denote modeled upper and lower anisotropy parameters, respectively. Conventions as in Figure 6. (b) Differential split times versus differential fast orientations for stations with more than six splits. The well-constrained two-layer anisotropic results with χ^2 no larger than 1.0 are indicated by circles, while less robust two-layer anisotropic results are denoted by diamonds. Symbols are color coded to the associated split time perturbations. (c) Anticorrelation between differential split times versus Moho depths from CRUST1.0 (Laske et al., 2013) underneath the same stations, where two-layer anisotropic results are color coded to their $\frac{\delta t_U}{\delta t_L}$ ratios. The gray dashed and solid lines denote the robust linear regression models with and without low-quality two-layer results marked by diamonds.

$\delta t_L - \delta t_U$ and $\frac{\delta t_U}{\delta t_L}$) and Moho depth as reflecting crustal imprints associated with compressional tectonics in western Laurentia (see section 4.3). In comparison, the weak link between the upper-layer splitting times and Moho depths (Figure S4a) suggests competing effects of other crustal growth/thickening mechanisms in western Laurentia such as mantle magmatic underplating (Gu et al., 2018, and references therein) that are not directly related to the tectonic strain. This provides a sensible explanation for the greatly enhanced splitting times along the foothills where the underlying crust has been significantly shortened and thickened since the Cretaceous orogenesis due to protracted North American craton-Canadian Cordillera convergence (e.g., Coney et al., 1980; DeCelles, 2004; Johnston, 2008; Monger & Price, 2002; Sigloch & Mihalynuk, 2013). Unfortunately, the origin of the anomalously larger apparent splitting times adjacent to the turning point of the STZ is poorly constrained because of the limited data from nearby stations TD01, TD02, TD03, and TD04; this prevented a reliable layered anisotropic modeling investigation.

4.3. Two Episodes of Collision-Related Compression in Western North America

The northwest trending upper-layer fast directions beneath the eastern central Alberta lithosphere represent fossil anisotropy (Figures 6 and 8a) that was (1) preserved during formation of the microcontinents in the

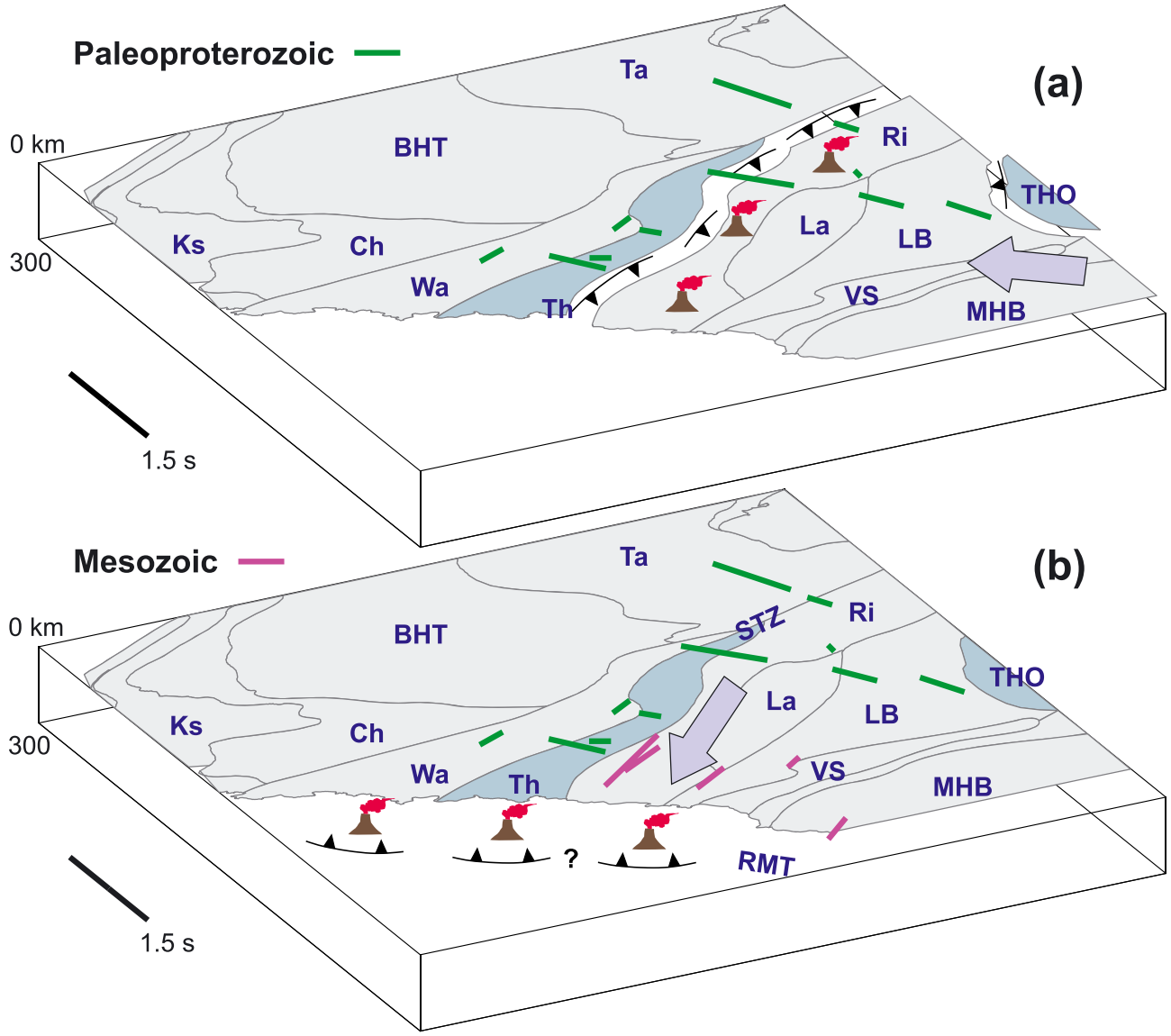

Figure 8. Cartoon showing formation of the frozen-in anisotropic fabrics whose directions are plotted at the sea level. (a) Fossil anisotropy (green bars) formed during the Paleoproterozoic amalgamation and the subsequent continental shortening of the Hearne-MHB-Wyoming (HMW) tectonic system. The Thorsby basin and the 2.0- to 1.8-Ga Trans-Hudson Orogen (THO) at the margin of the HMW are highlighted in turquoise. The black lines with filled triangles indicate convergence margins, and the purple arrow denotes the maximum strain direction in the HMW. (b) Fossil anisotropy (purple bars) resulted during the convergence associated with the formation of the North American Cordillera. The purple arrow indicates the maximum horizontal compressional direction associated with the Cordilleran orogenesis. Abbreviations and acronyms as in Figure 1.

region, (2) reworked by the ca. 1.9- to 1.8-Ga subduction along the eastern STZ due to the Rae-Hearne amalgamation along with the 2.0- to 1.8-Ga THO welding Hearne to Superior (Berman et al., 2007; Hoffman, 1988; Zhao et al., 2002), or (3) modified (again) by the postcollisional convergence involving the 2.0- to 1.8-Ga HMW tectonic system (the MHB and Wyoming are two Archean cratons extending from southern Alberta to Wyoming in the northern United States; e.g., Hoffman, 1988; Ross et al., 2000). The northern margin of the HMW (i.e., the STZ) reveals a quasi-linear anomalous Bouguer gravity low, indicating that the region had experienced significant crustal thickening (Gu et al., 2018). Evidence of convergence is revealed immediately south of the STZ, where 2.4-Ga gabbros were found in the Paleoproterozoic oceanic relic basin Thorsby and 1.78- to 1.85-Ga granitic rocks were documented in the magmatic arc (Rimbey; Ross et al., 1991). This is consistent with the distinctive high-velocity clusters beneath Wabamun and Hearne that

are separated by a low-shear-velocity zone extending down to ~80-km depth (Gu et al., 2016, 2018). A compressive tectonic regime is further indicated by seismic reflection imaging that revealed the crustal-scale imbrication with opposing dips on both sides of the Hearne province, that is, a northwestward dip under the Wabamun domain and a southeastward dip beneath the Hearne and Lacombe domains (Lucas et al., 1993; Ross et al., 2000). In the southern portion of the HMW, convergence was also indicated by 1.87-Ga subduction-related gneiss as well as the 1.77-Ga granulite facies metamorphism and partial melting along the Great Falls Tectonic Zone that welded the MHB and Wyoming together (e.g., Mueller et al., 2002; Sims et al., 2005). Given the widespread northwest trending upper-layer fast orientations across eastern central Alberta, which are approximately perpendicular to the Rimbey magmatic belt (Figure 8a), we suggest that these strain fabrics formed due to the long-lasting convergence associated with the 1.85- to 1.70-Ga formation of the HMW tectonic system, whose influence could also reach the Taltson orogenic belt (i.e., FMC).

It has long been recognized that the fast polarization of shear waves tends to occur along the maximum horizontal stress direction in the upper crust where vertically aligned cracks are developed (e.g., Crampin et al., 1984; Crampin & Chastin, 2003). Its potential crustal impact on seismic anisotropy (section 4.2) suggests that widespread upper crustal cracks could have formed in the HMW tectonic system in response to the northwest oriented stress field during the Paleoproterozoic amalgamation of the HMW system. This compression could also have deformed some portions of the underlying lithospheric mantle where the a-axes of olivine aggregates were entrained in a northwest trending horizontal foliation plane, resulting in the coherent postcollisional deformation of the HMW continental lithosphere (i.e., crust and upper mantle). Further insight on lithosphere deformation coupling could be gained by quantifying the crustal anisotropy utilizing both splitting and azimuthal variations of the Moho *P*-to-*S* converted wave (i.e., *Ps* phase) from teleseismic receiver functions (e.g., Savage, 1998; Schulte-Pelkum & Mahan, 2014; Wu et al., 2015).

The northeast oriented upper-layer anisotropic directions in Wabamun significantly deviate from the northwest trending counterparts south of the STZ, which highlight the presence and geometry of this important Paleoproterozoic tectonic boundary. This clear transition in the frozen-in upper-layer fabrics implies that Wabamun was not a part of the tectonic vise that led to the southeast dip of the imbricated Thorsby basin (Ross et al., 2000). Given the resemblance to the present-day maximum compressive crustal stress direction (Heidbach et al., 2016; Wang et al., 2017), one could argue that the observed northeast trending fabrics could represent the crustal strain as a result of the stress-aligned shape-preferred orientation of isotropic elastic materials such as melt pockets or crustal cracks (Crampin & Chastin, 2003; Long & Becker, 2010). However, this scenario cannot explain the widespread crustal thickening adjacent to the STZ or the sharp transition in the deformation mechanism south of the STZ.

Despite the ongoing debate concerning the kinematic assembly of Cordilleran North America such as the polarity of subduction leading to the Late Jurassic–Late Cretaceous Cordilleran arc magmatism (e.g., Coney et al., 1980; DeCelles, 2004; Johnston, 2008; Monger & Price, 2002; Sigloch & Mihalynuk, 2013), it has been widely accepted that the Cordillera formed as the result of the sequential convergence between multiple magmatic arc terranes and western Laurentia that had been drifting westward since the Early Jurassic time (e.g., Seton et al., 2012; Wu et al., 2017). The long-lasting compression that accumulated along the Cordilleran collisional margin could have produced the northeasterly upper-layer fabrics along the foothills (Figures 6 and 8b), which could also have originated from coherent crustal and lithospheric mantle anisotropy (Figure 7c). However, the impact of the Cordilleran orogenesis appears to be spatially confined along the southwestern margin of western Laurentia.

5. Conclusions

In this study, we analyzed the shear wave splitting for core transiting phases recorded by 82 stations in Alberta, yielding a predominantly northeast trending fast polarization direction with an average of 54.6° ± 17.2° along with an average split time of 1.1 ± 0.3 s. Two-layered modeling for stations with more than six splitting measurements revealed lower-layer fast orientations that were roughly parallel to the present-day plate motion directions across Alberta, which we interpret as resulting from ongoing shear deformation at asthenospheric depths. Along the Rocky Mountains foothills, the lower-layer anisotropy directions deviate from the surface plate motion directions, potentially indicating disrupted mantle flow due to the complex LAB beneath the foothills. Two episodes of collision-related convergence likely caused

the distinct upper-layer anisotropic patterns. The STZ is bounded by the northwesterly fabrics across central eastern Alberta and the northeast trending fabrics in Wabamun. The former directions could have resulted from continental convergence during the Paleoproterozoic formation of the HMW tectonic system. The northeasterly upper-layer fabrics along the foothills are parallel to the maximum compressional crustal stress direction, suggesting a postcollisional convergence origin associated with the Cordilleran orogenesis since the Late Cretaceous.

Acknowledgments
Splitting measurements are listed in the supporting information. Seismic data for networks USArray and RAVEN, TD, and XR are distributed by the IRIS Data Management Center (https://ds.iris.edu/ds/nodes/dmc/). Seismic data from the Canadian National Seismographic Network (CNSN) can be requested from the Canadian National Data Center (https://www.earthquakescanada.nrcan.gc.ca/stndon/CNDC/index-en.php). Event data for all shear wave splitting measurements can be accessed through the website https://sites.google.com/a/ualberta.ca/seisworld/data/shear-wave-splitting. We thank Editor Martha Savage and Associate Editor Kelly H. Liu for handling this manuscript. We are grateful for the constructive comments from reviewer Stephen S. Gao and an anonymous reviewer that allowed us to significantly improve upon an earlier version of this manuscript. We thank Corné Kreemer for sharing his latest geodetic global plate motion, Ruijia Wang for providing focal mechanisms in Alberta, and Mitch Liddell for his assistance with forward-modeling two-layer anisotropy. This study was supported by the National Key R&D Program of China grant 2016YFC0600407, the Natural Sciences and Engineering Research Council of Canada grant RES0029444, "Future Energy Systems" funds at the University of Alberta and the Australian Research Council grant FL150100133.

References

Amante, C., & Eakins, B. W. (2009). ETOPO1 1 arc-minute global relief model: Procedures, data sources and analysis. U.S. Department of Commerce, National Oceanic and Atmospheric Administration, National Environmental Satellite, Data, and Information Service, National Geophysical Data Center, Marine Geology and Geophysics Division Colorado.

Anderson, D. L. (2007). *New theory of the Earth*. Cambridge, UK: Cambridge University Press. https://doi.org/10.1017/CBO9781139167291

Aulbach, S., Griffin, W., O'Reilly, S., & McCandless, T. E. (2004). Genesis and evolution of the lithospheric mantle beneath the Buffalo Head Terrane, Alberta (Canada). *Lithos*, *77*(1-4), 413–451. https://doi.org/10.1016/j.lithos.2004.04.020

Bally, A. W., Gordy, P., & Stewart, G. A. (1966). Structure, seismic data, and orogenic evolution of southern Canadian Rocky Mountains. *Bulletin of Canadian Petroleum Geology*, *14*(3), 337–381.

Bao, X., & Eaton, D. W. (2015). Large variations in lithospheric thickness of western Laurentia: Tectonic inheritance or collisional reworking? *Precambrian Research*, *266*, 579–586. https://doi.org/10.1016/j.precamres.2015.05.010

Bao, X., Eaton, D. W., & Gu, Y. J. (2016). Rayleigh wave azimuthally anisotropic phase velocity maps beneath western Canada. *Journal of Geophysical Research: Solid Earth*, *121*, 1821–1834. https://doi.org/10.1002/2015JB012453

Bastow, I. D., Thompson, D. A., Wookey, J., Kendall, J.-M., Helffrich, G., Snyder, D. B., et al. (2011). Precambrian plate tectonics: Seismic evidence from northern Hudson Bay, Canada. *Geology*, *39*(1), 91–94. https://doi.org/10.1130/G31396.1

Beaumont, C. (1981). Foreland basins. *Geophysical Journal of the Royal Astronomical Society*, *65*(2), 291–329. https://doi.org/10.1111/j.1365-246X.1981.tb02715.x

Becker, T. W., Kellogg, J. B., Ekström, G., & O'Connell, R. J. (2003). Comparison of azimuthal seismic anisotropy from surface waves and finite strain from global mantle-circulation models. *Geophysical Journal International*, *155*(2), 696–714. https://doi.org/10.1046/j.1365-246X.2003.02085.x

Bell, J., & Bachu, S. (2003). In situ stress magnitude and orientation estimates for Cretaceous coal-bearing strata beneath the plains area of central and southern Alberta. *Bulletin of Canadian Petroleum Geology*, *51*(1), 1–28. https://doi.org/10.2113/gscpgbull.51.1.1

Bell, J., & Gough, D. (1979). Northeast-southwest compressive stress in Alberta evidence from oil wells. *Earth and Planetary Science Letters*, *45*(2), 475–482. https://doi.org/10.1016/0012-821X(79)90146-8

Berman, R., Davis, W., & Pehrsson, S. (2007). Collisional Snowbird Tectonic Zone resurrected: Growth of Laurentia during the 1.9 Ga accretionary phase of the Hudsonian orogeny. *Geology*, *35*(10), 911–914. https://doi.org/10.1130/G23771A.1

Bird, P. (2003). An updated digital model of plate boundaries. *Geochemistry, Geophysics, Geosystems*, *4*(3), 1027. https://doi.org/10.1029/2001GC000252

Boerner, D., Kurtz, R., Craven, J., Ross, G., & Jones, F. (2000). A synthesis of electromagnetic studies in the Lithoprobe Alberta Basement Transect: Constraints on Paleoproterozoic indentation tectonics. *Canadian Journal of Earth Sciences*, *37*(11), 1509–1534. https://doi.org/10.1139/e00-063

Bokelmann, G. H., & Silver, P. G. (2002). Shear stress at the base of shield lithosphere. *Geophysical Research Letters*, *29*(23), 2091. https://doi.org/10.1029/2002GL015925

Bowman, J. R., & Ando, M. (1987). Shear-wave splitting in the upper-mantle wedge above the Tonga subduction zone. *Geophysical Journal International*, *88*(1), 25–41. https://doi.org/10.1111/j.1365-246X.1987.tb01367.x

Chen, Y., Gu, Y. J., Dokht, R. M., & Sacchi, M. D. (2015). Crustal imprints of Precambrian orogenesis in western Laurentia. *Journal of Geophysical Research: Solid Earth*, *120*, 6993–7012. https://doi.org/10.1002/2014JB011353

Chen, Y., Gu, Y. J., & Hung, S. H. (2017). Finite-frequency P-wave tomography of the Western Canada Sedimentary Basin: Implications for the lithospheric evolution in western Laurentia. *Tectonophysics*, *698*, 79–90. https://doi.org/10.1016/j.tecto.2017.01.006

Chen, Y., Gu, Y. J., & Hung, S. H. (2018). A new appraisal of lithospheric structures of the Cordillera-Craton Boundary Region in Western Canada. *Tectonics*, *37*, 3207–3228. https://doi.org/10.1029/2018TC004956

Chevrot, S. (2000). Multichannel analysis of shear wave splitting. *Journal of Geophysical Research*, *105*(B9), 21,579–21,590. https://doi.org/10.1029/2000JB900199

Cimini, G. B., & De Gori, P. (2001). Nonlinear *P*-wave tomography of subducted lithosphere beneath central-southern Apennines (Italy). *Geophysical Research Letters*, *28*(23), 4387–4390. https://doi.org/10.1029/2001GL013546

Clowes, R. M., Burianyk, M. J., Gorman, A. R., & Kanasewich, E. R. (2002). Crustal velocity structure from SAREX, the southern Alberta refraction experiment. *Canadian Journal of Earth Sciences*, *39*(3), 351–373. https://doi.org/10.1139/e01-070

Coney, P. J., Jones, D. L., & Monger, J. W. (1980). Cordilleran suspect terranes. *Nature*, *288*(5789), 329–333. https://doi.org/10.1038/288329a0

Conrad, C. P., Behn, M. D., & Silver, P. G. (2007). Global mantle flow and the development of seismic anisotropy: Differences between the oceanic and continental upper mantle. *Journal of Geophysical Research*, *112*, B07317. https://doi.org/10.1029/2006JB004608

Cook, F. A. (1995). Lithospheric processes and products in the southern Canadian Cordillera: A Lithoprobe perspective. *Canadian Journal of Earth Sciences*, *32*(10), 1803–1824. https://doi.org/10.1139/e95-139

Corrigan, D., Pehrsson, S., Wodicka, N., & De Kemp, E. (2009). The Palaeoproterozoic Trans-Hudson Orogen: A prototype of modern accretionary processes. *Geological Society, London, Special Publications*, *327*(1), 457–479. https://doi.org/10.1144/SP327.19

Courtier, A. M., Gaherty, J. B., Revenaugh, J., Bostock, M. G., & Garnero, E. J. (2010). Seismic anisotropy associated with continental lithosphere accretion beneath the CANOE array, northwestern Canada. *Geology*, *38*(10), 887–890. https://doi.org/10.1130/G31120.1

Crampin, S., & Chastin, S. (2003). A review of shear wave splitting in the crack-critical crust. *Geophysical Journal International*, *155*(1), 221–240. https://doi.org/10.1046/j.1365-246X.2003.02037.x

Crampin, S., Chesnokov, E. M., & Hipkin, R. G. (1984). Seismic anisotropy—The state of the art: II. *Geophysical Journal International*, *76*(1), 1–16. https://doi.org/10.1111/j.1365-246X.1984.tb05017.x

Currie, C. A., Cassidy, J. F., Hyndman, R. D., & Bostock, M. G. (2004). Shear wave anisotropy beneath the Cascadia subduction zone and western North American craton. *Geophysical Journal International*, *157*(1), 341–353. https://doi.org/10.1111/j.1365-246X.2004.02175.x

Dalton, C. A., & Gaherty, J. B. (2013). Seismic anisotropy in the continental crust of northwestern Canada. *Geophysical Journal International*, *193*(1), 338–348. https://doi.org/10.1093/gji/ggs108

Dalton, C. A., Gaherty, J. B., & Courtier, A. M. (2011). Crustal VS structure in northwestern Canada: Imaging the Cordillera-craton transition with ambient noise tomography. *Journal of Geophysical Research*, *116*, B12315. https://doi.org/10.1029/2011JB008499

Darbyshire, F., Bastow, I., Petrescu, L., Gilligan, A., & Thompson, D. (2017). A tale of two orogens: Crustal processes in the Proterozoic Trans-Hudson and Grenville Orogens, eastern Canada. *Tectonics*, *36*, 1633–1659. https://doi.org/10.1002/2017TC004479

Darbyshire, F. A., Eaton, D. W., & Bastow, I. D. (2013). Seismic imaging of the lithosphere beneath Hudson Bay: Episodic growth of the Laurentian mantle keel. *Earth and Planetary Science Letters*, *373*, 179–193. https://doi.org/10.1016/j.epsl.2013.05.002

DeCelles, P. G. (2004). Late Jurassic to Eocene evolution of the Cordilleran thrust belt and foreland basin system, western USA. *American Journal of Science*, *304*(2), 105–168. https://doi.org/10.2475/ajs.304.2.105

Eaton, D. W., & Cassidy, J. F. (1996). A relic Proterozoic subduction zone in western Canada: New evidence from seismic reflection and receiver function data. *Geophysical Research Letters*, *23*(25), 3791–3794. https://doi.org/10.1029/96GL03619

Eaton, D. W., Ross, G. M., & Clowes, R. M. (1999). Seismic-reflection and potential-field studies of the Vulcan structure, western Canada: A Paleoproterozoic Pyrenees? *Journal of Geophysical Research*, *104*(B10), 23,255–23,269. https://doi.org/10.1029/1999JB900204

Eaton, D. W., Ross, G. M., Cook, F. A., & VanderVelden, A. (2000). Seismic imaging of the upper mantle beneath the Rocky Mountain foreland, southwestern Alberta. *Canadian Journal of Earth Sciences*, *37*(11), 1493–1507. https://doi.org/10.1139/e00-068

Flesch, L. M., Holt, W. E., Haines, A. J., Wen, L., & Shen-Tu, B. (2007). The dynamics of western North America: Stress magnitudes and the relative role of gravitational potential energy, plate interaction at the boundary and basal tractions. *Geophysical Journal International*, *169*(3), 866–896. https://doi.org/10.1111/j.1365-246X.2007.03274.x

Flowers, R., Bowring, S., & Williams, M. (2006). Timescales and significance of high-pressure, high-temperature metamorphism and mafic dike anatexis, Snowbird Tectonic Zone, Canada. *Contributions to Mineralogy and Petrology*, *151*(5), 558–581. https://doi.org/10.1007/s00410-006-0066-7

Fouch, M. J., Fischer, K. M., Parmentier, E., Wysession, M. E., & Clarke, T. J. (2000). Shear wave splitting, continental keels, and patterns of mantle flow. *Journal of Geophysical Research*, *105*(B3), 6255–6275. https://doi.org/10.1029/1999JB900372

Fouch, M. J., & Rondenay, S. (2006). Seismic anisotropy beneath stable continental interiors. *Physics of the Earth and Planetary Interiors*, *158*(2-4), 292–320. https://doi.org/10.1016/j.pepi.2006.03.024

Gao, S. S., & Liu, K. H. (2009). Significant seismic anisotropy beneath the southern Lhasa Terrane, Tibetan Plateau. *Geochemistry, Geophysics, Geosystems*, *10*, Q02008. https://doi.org/10.1029/2008GC002227

Gorman, A. R., Clowes, R. M., Ellis, R. M., Henstock, T. J., Spence, G. D., Keller, G. R., et al. (2002). Deep Probe: Imaging the roots of western North America. *Canadian Journal of Earth Sciences*, *39*(3), 375–398. https://doi.org/10.1139/e01-064

Gripp, A. E., & Gordon, R. G. (2002). Young tracks of hotspots and current plate velocities. *Geophysical Journal International*, *150*(2), 321–361. https://doi.org/10.1046/j.1365-246X.2002.01627.x

Gu, Y., Chen, Y., & Hung, S. (2016). P and S wave finite-frequency imaging of the Cordillera-craton Boundary Zone in Western Canada. In AGU Fall Meeting Abstracts.

Gu, Y. J., Chen, Y., Dokht, R. M., & Wang, R. (2018). Precambrian tectonic discontinuities in western Laurentia: Broadband seismological perspectives on the Snowbird and Great Falls Tectonic Zones. *Tectonics*, *37*, 1411–1434. https://doi.org/10.1029/2017TC004843

Gu, Y. J., Okeler, A., Shen, L., & Contenti, S. (2011). The Canadian Rockies and Alberta Network (CRANE): New constraints on the Rockies and western Canada sedimentary basin. *Seismological Research Letters*, *82*(4), 575–588. https://doi.org/10.1785/gssrl.82.4.575

Gu, Y. J., Zhang, Y., Sacchi, M. D., Chen, Y., & Contenti, S. (2015). Sharp mantle transition from cratons to cordillera in southwestern Canada. *Journal of Geophysical Research: Solid Earth*, *120*, 5051–5069. https://doi.org/10.1002/2014JB011802

Gung, Y., Panning, M., & Romanowicz, B. (2003). Global anisotropy and the thickness of continents. *Nature*, *422*(6933), 707–711. https://doi.org/10.1038/nature01559

Hanmer, S., Williams, M., & Kopf, C. (1995). Striding-Athabasca mylonite zone: Implications for the Archean and Early Proterozoic tectonics of the western Canadian Shield. *Canadian Journal of Earth Sciences*, *32*(2), 178–196. https://doi.org/10.1139/e95-015

Harper, J. (1986). Mantle flow and plate motions. *Geophysical Journal International*, *87*(1), 155–171. https://doi.org/10.1111/j.1365-246X.1986.tb04551.x

Heidbach, O., Rajabi, M., Reiter, K., Ziegler, M., and the WSM Team (2016). World stress map database release 2016. Technical report, GFZ Data Services.

Hoffman, P. F. (1988). United plates of America, the birth of a craton: Early Proterozoic assembly and growth of Laurentia. *Annual Review of Earth and Planetary Sciences*, *16*(1), 543–603. https://doi.org/10.1146/annurev.ea.16.050188.002551

Hope, J., Eaton, D. W., & Ross, G. M. (1999). Lithoprobe seismic transect of the Alberta Basin: Compilation and overview. *Bulletin of Canadian Petroleum Geology*, *47*(4), 331–345.

Johnston, S. T. (2008). The cordilleran ribbon continent of North America. *Annual Review of Earth and Planetary Sciences*, *36*(1), 495–530. https://doi.org/10.1146/annurev.earth.36.031207.124331

Kennett, B., & Engdahl, E. (1991). Traveltimes for global earthquake location and phase identification. *Geophysical Journal International*, *105*(2), 429–465. https://doi.org/10.1111/j.1365-246X.1991.tb06724.x

Kreemer, C., Blewitt, G., & Klein, E. C. (2014). A geodetic plate motion and global strain rate model. *Geochemistry, Geophysics, Geosystems*, *15*, 3849–3889. https://doi.org/10.1002/2014GC005407

Laske, G., Masters, G., Ma, Z., and Pasyanos, M. (2013). Update on CRUST1. 0—A 1-degree global model of Earth's crust. In Geophys. Res. Abstr., volume 15, page 2658.

Leary, P., Li, Y., & Aki, K. (1987). Observation and modelling of fault-zone fracture seismic anisotropy-I. P, SV and SH travel times. *Geophysical Journal International*, *91*(2), 461–484. https://doi.org/10.1111/j.1365-246X.1987.tb05239.x

Liddell, M. V., Bastow, I., Darbyshire, F., Gilligan, A., & Pugh, S. (2017). The formation of Laurentia: Evidence from shear wave splitting. *Earth and Planetary Science Letters*, *479*, 170–178. https://doi.org/10.1016/j.epsl.2017.09.030

Liu, K. H., Elsheikh, A., Lemnifi, A., Purevsuren, U., Ray, M., Refayee, H., et al. (2014). A uniform database of teleseismic shear wave splitting measurements for the western and central United States. *Geochemistry, Geophysics, Geosystems*, *15*, 2075–2085. https://doi.org/10.1002/2014GC005267

Liu, L., Gurnis, M., Seton, M., Saleeby, J., Müller, R. D., & Jackson, J. M. (2010). The role of oceanic plateau subduction in the Laramide orogeny. *Nature Geoscience*, *3*(5), 353–357. https://doi.org/10.1038/ngeo829

Long, M. D., & Becker, T. W. (2010). Mantle dynamics and seismic anisotropy. *Earth and Planetary Science Letters*, *297*(3-4), 341–354. https://doi.org/10.1016/j.epsl.2010.06.036

Long, M. D., & Silver, P. G. (2009). Shear wave splitting and mantle anisotropy: Measurements, interpretations, and new directions. *Surveys in Geophysics*, *30*(4–5), 407–461. https://doi.org/10.1007/s10712-009-9075-1

Lucas, S., Green, A., Hajnal, Z., White, D., Lewry, J., Ashton, K., et al. (1993). Deep seismic profile across a Proterozoic collision zone: Surprises at depth. *Nature*, *363*(6427), 339–342. https://doi.org/10.1038/363339a0

Mahan, K., & Williams, M. (2005). Reconstruction of a large deep-crustal terrane: Implications for the Snowbird Tectonic Zone and early growth of Laurentia. *Geology*, *33*(5), 385–388. https://doi.org/10.1130/G21273.1

Marone, F., & Romanowicz, B. (2007). The depth distribution of azimuthal anisotropy in the continental upper mantle. *Nature*, *447*(7141), 198–201. https://doi.org/10.1038/nature05742

McKenzie, D. (1979). Finite deformation during fluid flow. *Geophysical Journal International*, *58*(3), 689–715. https://doi.org/10.1111/j.1365-246X.1979.tb04803.x

Monger, J., & Price, R. (2002). The Canadian Cordillera: Geology and tectonic evolution. *CSEG Recorder*, *27*(2), 17–36.

Mossop, G., & Shetsen, I. (1994). Introduction to the geological atlas of the Western Canada Sedimentary Basin. *Geological atlas of the Western Canadian Sedimentary Basin*. Compiled by G. D. Mossop and I. Shetson. Canadian Society of Petroleum Geologists and Alberta Research Council, Calgary, Alberta, pp. 1–12.

Mueller, P., & Frost, C. D. (2006). The Wyoming Province: A distinctive Archean craton in Laurentian North America. *Canadian Journal of Earth Sciences*, *43*(10), 1391–1397. https://doi.org/10.1139/e06-075

Mueller, P. A., Heatherington, A. L., Kelly, D. M., Wooden, J. L., & Mogk, D. W. (2002). Paleoproterozoic crust within the Great Falls Tectonic Zone: Implications for the assembly of southern Laurentia. *Geology*, *30*(2), 127–130. https://doi.org/10.1130/0091-7613(2002)030<0127:PCWTGF>2.0.CO;2

Nettles, M., & Dziewoński, A. M. (2008). Radially anisotropic shear velocity structure of the upper mantle globally and beneath North America. *Journal of Geophysical Research*, *113*, B02303. https://doi.org/10.1029/2006JB004819

Nieuwenhuis, G., Unsworth, M. J., Pana, D., Craven, J., & Bertrand, E. (2014). Three-dimensional resistivity structure of Southern Alberta, Canada: Implications for Precambrian tectonics. *Geophysical Journal International*, *197*(2), 838–859. https://doi.org/10.1093/gji/ggu068

Ökeler, A., Gu, Y. J., Lerner-Lam, A., & Steckler, M. S. (2009). Seismic structure of the southern Apennines as revealed by waveform modelling of regional surface waves. *Geophysical Journal International*, *178*(3), 1473–1492. https://doi.org/10.1111/j.1365-246X.2009.04229.x

Park, J., & Levin, V. (2002). Seismic anisotropy: Tracing plate dynamics in the mantle. *Science*, *296*(5567), 485–489. https://doi.org/10.1126/science.1067319

Pasyanos, M. E., Masters, T. G., Laske, G., & Ma, Z. (2014). LITHO1. 0: An updated crust and lithospheric model of the Earth. *Journal of Geophysical Research: Solid Earth*, *119*, 2153–2173. https://doi.org/10.1002/2013JB010626

Pilkington, M., Miles, W., Ross, G., & Roest, W. (2000). Potential-field signatures of buried Precambrian basement in the Western Canada Sedimentary Basin. *Canadian Journal of Earth Sciences*, *37*(11), 1453–1471. https://doi.org/10.1139/e00-020

Price, R. (1981). The cordilleran foreland thrust and fold belt in the southern Canadian Rocky Mountains. *Geological Society, London, Special Publications*, *9*(1), 427–448. https://doi.org/10.1144/GSL.SP.1981.009.01.39

Reed, C. A., Liu, K. H., Yu, Y., & Gao, S. S. (2017). Seismic anisotropy and mantle dynamics beneath the Malawi Rift Zone, East Africa. *Tectonics*, *36*, 1338–1351. https://doi.org/10.1002/2017TC004519

Reiter, K., Heidbach, O., Schmitt, D., Haug, K., Ziegler, M., & Moeck, I. (2014). A revised crustal stress orientation database for Canada. *Tectonophysics*, *636*, 111–124. https://doi.org/10.1016/j.tecto.2014.08.006

Ross, G., McNicoll, V., Geldsetzer, H., Parrish, R., Carr, S., & Kinsman, A. (1993). Detrital zircon geochronology of Siluro-Devonian sandstones, Rocky Mountains, northeastern British Columbia. *Bulletin of Canadian Petroleum Geology*, *41*(3), 349–357.

Ross, G., Parrish, R., Villeneuve, M., & Bowring, S. (1991). Geophysics and geochronology of the crystalline basement of the Alberta Basin, western Canada. *Canadian Journal of Earth Sciences*, *28*(4), 512–522. https://doi.org/10.1139/e91-045

Ross, G. M. (2002). Evolution of Precambrian continental lithosphere in Western Canada: Results from Lithoprobe studies in Alberta and beyond. *Canadian Journal of Earth Sciences*, *39*(3), 413–437. https://doi.org/10.1139/e02-012

Ross, G. M., & Eaton, D. W. (2002). Proterozoic tectonic accretion and growth of western Laurentia: Results from Lithoprobe studies in Northern Alberta. *Canadian Journal of Earth Sciences*, *39*(3), 313–329. https://doi.org/10.1139/e01-081

Ross, G. M., Eaton, D. W., Boerner, D. E., & Miles, W. (2000). Tectonic entrapment and its role in the evolution of continental lithosphere: An example from the Precambrian of western Canada. *Tectonics*, *19*(1), 116–134. https://doi.org/10.1029/1999TC900047

Savage, M. (1999). Seismic anisotropy and mantle deformation: What have we learned from shear wave splitting? *Reviews of Geophysics*, *37*(1), 65–106. https://doi.org/10.1029/98RG02075

Savage, M. K. (1998). Lower crustal anisotropy or dipping boundaries? Effects on receiver functions and a case study in New Zealand. *Journal of Geophysical Research*, *103*(B7), 15,069–15,087. https://doi.org/10.1029/98JB00795

Schulte-Pelkum, V., & Mahan, K. H. (2014). A method for mapping crustal deformation and anisotropy with receiver functions and first results from USArray. *Earth and Planetary Science Letters*, *402*, 221–233. https://doi.org/10.1016/j.epsl.2014.01.050

Schulte-Pelkum, V., Mahan, K. H., Shen, W., & Stachnik, J. C. (2017). The distribution and composition of high-velocity lower crust across the continental US: Comparison of seismic and xenolith data and implications for lithospheric dynamics and history. *Tectonics*, *36*, 1455–1496. https://doi.org/10.1002/2017TC004480

Seton, M., Müller, R. D., Zahirovic, S., Gaina, C., Torsvik, T., Shephard, G., et al. (2012). Global continental and ocean basin reconstructions since 200 Ma. *Earth-Science Reviews*, *113*(3–4), 212–270. https://doi.org/10.1016/j.earscirev.2012.03.002

Shragge, J., Bostock, M., Bank, C. G., & Ellis, R. (2002). Integrated teleseismic studies of the southern Alberta upper mantle. *Canadian Journal of Earth Sciences*, *39*(3), 399–411. https://doi.org/10.1139/e01-084

Sigloch, K., & Mihalynuk, M. G. (2013). Intra-oceanic subduction shaped the assembly of Cordilleran North America. *Nature*, *496*(7443), 50–56. https://doi.org/10.1038/nature12019

Silver, P. G. (1996). Seismic anisotropy beneath the continents: Probing the depths of geology. *Annual Review of Earth and Planetary Sciences*, *24*(1), 385–432. https://doi.org/10.1146/annurev.earth.24.1.385

Silver, P. G., & Chan, W. W. (1991). Shear wave splitting and subcontinental mantle deformation. *Journal of Geophysical Research*, *96*(B10), 16,429–16,454. https://doi.org/10.1029/91JB00899

Silver, P. G., & Savage, M. K. (1994). The interpretation of shear-wave splitting parameters in the presence of two anisotropic layers. *Geophysical Journal International*, *119*(3), 949–963. https://doi.org/10.1111/j.1365-246X.1994.tb04027.x

Sims, P. K., Lund, K., and Anderson, E. (2005). Precambrian crystalline basement map of Idaho—An interpretation of aeromagnetic anomalies. Technical report.

Turner, G., & Gough, D. (1983). Magnetic fabric, strain and paleostress in the Canadian Rocky Mountains. *Tectonophysics*, *96*(3–4), 311–330. https://doi.org/10.1016/0040-1951(83)90224-X

van der Lee, S., & Frederiksen, A. (2005). Surface wave tomography applied to the North American upper mantle. In A. Levander & G. Nolet (Eds.), *Seismic Earth: Array analysis of broadband seismograms* (pp. 67–80). Washington, DC: American Geophysical Union.

Villeneuve, M., Ross, G., Theriault, R., and Miles, W. (1993). Tectonic subdivision and U-Pb geochronology of the crystalline basement of the Alberta Basin, western Canada. Ottawa.

Walker, A. M., & Wookey, J. (2012). MSAT—A new toolkit for the analysis of elastic and seismic anisotropy. *Computers & Geosciences*, *49*, 81–90. https://doi.org/10.1016/j.cageo.2012.05.031

Wang, R., Gu, Y. J., & Zhang, M. (2017). Hydraulic fracturing induced seismicity in western Canada: insights from focal mechanism and swarm analysis. In *2017 workshop: Microseismic technologies and applications* (pp. 42–45). Hefei, China: Society of Exploration Geophysicists.

Ward, D., Mahan, K., & Schulte-Pelkum, V. (2012). Roles of quartz and mica in seismic anisotropy of mylonites. *Geophysical Journal International*, *190*(2), 1123–1134. https://doi.org/10.1111/j.1365-246X.2012.05528.x

Wolfe, C. J., & Silver, P. G. (1998). Seismic anisotropy of oceanic upper mantle: Shear wave splitting methodologies and observations. *Journal of Geophysical Research*, *103*(B1), 749–771. https://doi.org/10.1029/97JB02023

Wu, J., Zhang, Z., Kong, F., Yang, B. B., Yu, Y., Liu, K. H., & Gao, S. S. (2015). Complex seismic anisotropy beneath western Tibet and its geodynamic implications. *Earth and Planetary Science Letters*, *413*, 167–175. https://doi.org/10.1016/j.epsl.2015.01.002

Wu, L., Kravchinsky, V. A., Gu, Y. J., & Potter, D. K. (2017). Absolute reconstruction of the closing of the Mongol-Okhotsk Ocean in the Mesozoic elucidates the genesis of the slab geometry underneath Eurasia. *Journal of Geophysical Research: Solid Earth*, *122*, 4831–4851. https://doi.org/10.1002/2017JB014261

Wüstefeld, A., & Bokelmann, G. (2007). Null detection in shear-wave splitting measurements. *Bulletin of the Seismological Society of America*, *97*(4), 1204–1211. https://doi.org/10.1785/0120060190

Wüstefeld, A., Bokelmann, G., Zaroli, C., & Barruol, G. (2008). SplitLab: A shear-wave splitting environment in Matlab. *Computers & Geosciences*, *34*(5), 515–528. https://doi.org/10.1016/j.cageo.2007.08.002

Yuan, H., & Romanowicz, B. (2010). Lithospheric layering in the North American craton. *Nature*, *466*(7310), 1063–1068. https://doi.org/10.1038/nature09332

Zhao, G., Cawood, P. A., Wilde, S. A., & Sun, M. (2002). Review of global 2.1–1.8 Ga orogens: Implications for a pre-Rodinia supercontinent. *Earth-Science Reviews*, *59*(1–4), 125–162. https://doi.org/10.1016/S0012-8252(02)00073-9